Evaluating triple oxygen isotope estimates of gross primary production at the Hawaii Ocean Time-series and Bermuda Atlantic Time-series Study sites

David P. Nicholson,[1] Rachel H. R. Stanley,[1] Eugeni Barkan,[2] David M. Karl,[3] Boaz Luz,[2] Paul D. Quay,[4] and Scott C. Doney[1]

Received 2 December 2010; revised 19 March 2012; accepted 20 March 2012; published 8 May 2012.

[1] The triple oxygen isotopic composition of dissolved oxygen ($^{17}\Delta$) is a promising tracer of gross oxygen productivity (*P*) in the ocean. Recent studies have inferred a high and variable ratio of *P* to ^{14}C net primary productivity (12–24 h incubations) (e.g., *P*:NPP(^{14}C) of 5–10) using the $^{17}\Delta$ tracer method, which implies a very low efficiency of phytoplankton growth rates relative to gross photosynthetic rates. We added oxygen isotopes to a one-dimensional mixed layer model to assess the role of physical dynamics in potentially biasing estimates of *P* using the $^{17}\Delta$ tracer method at the Bermuda Atlantic Time-series Study (BATS) and Hawaii Ocean Time-series (HOT). Model results were compared to multiyear observations at each site. Entrainment of high $^{17}\Delta$ thermocline water into the mixed layer was the largest source of error in estimating *P* from mixed layer $^{17}\Delta$. At both BATS and HOT, entrainment bias was significant throughout the year and resulted in an annually averaged overestimate of mixed layer *P* of 60 to 80%. When the entrainment bias is corrected for, *P* calculated from observed $^{17}\Delta$ and ^{14}C productivity incubations results in a gross:net productivity ratio of 2.6 (+0.9 −0.8) at BATS. At HOT a gross:net ratio decreasing linearly from 3.0 (+1.0 −0.8) at the surface to 1.4 (+0.6 −0.6) at depth best reproduced observations. In the seasonal thermocline at BATS, however, a significantly higher gross:net ratio or large lateral fluxes of $^{17}\Delta$ must be invoked to explain $^{17}\Delta$ field observations.

Citation: Nicholson, D. P., R. H. R. Stanley, E. Barkan, D. M. Karl, B. Luz, P. D. Quay, and S. C. Doney (2012), Evaluating triple oxygen isotope estimates of gross primary production at the Hawaii Ocean Time-series and Bermuda Atlantic Time-series Study sites, *J. Geophys. Res.*, *117*, C05012, doi:10.1029/2010JC006856.

1. Introduction

[2] Quantifying rates of gross primary productivity and respiration by primary producers in the ocean is fundamentally important for developing a mechanistic understanding of how marine ecosystems function, including energy transduction and elemental cycling. Such an understanding is necessary in order to predict changes in ecosystem structure and carbon cycle feedbacks in the face of rising CO_2 and a changing climate.

[3] To assess the global distribution of marine primary productivity and make projections for the future, we rely on satellite based primary productivity algorithms (SatPPMs) and marine biogeochemical models (BOGCMs) [*Doney et al.*, 2009; *Friedrichs et al.*, 2009]. The performance of these models, however, has primarily been assessed through comparison to primary productivity measurements based only on ^{14}C labeled bottle incubations, a method which has a number of known limitations [*Harrison and Harris*, 1986; *Marra*, 2002; *Peterson*, 1980]. At the Bermuda Atlantic Time-series Study (BATS) and Hawaii Ocean Time-series (HOT) such model intercomparisons show that, while improving, both SatPPMs and BOGCMs fail to accurately capture observed variability and long-term trends in primary productivity [*Saba et al.*, 2010]. The use of other measures of ecosystem metabolism has been limited primarily by the availability of widespread data using other methods. The development and adoption of new tracers, such as triple oxygen isotopes [*Luz and Barkan*, 2000; *Luz et al.*, 1999], fast repetition rate fluorometry (FRRF) [*Kolber et al.*, 1998] and O_2/Ar ratios [*Craig and Hayward*, 1987; *Emerson*, 1987; *Spitzer and Jenkins*, 1989], have improved our ability to access multiple aspects of upper ocean community metabolism. While each tracer has its shortcomings, together they

[1]Marine Chemistry and Geochemistry Department, Woods Hole Oceanographic Institution, Woods Hole, Massachusetts, USA.
[2]Institute of Earth Sciences, Hebrew University of Jerusalem, Jerusalem, Israel.
[3]Department of Oceanography, University of Hawai'i at Mānoa, Honolulu, Hawaii, USA.
[4]School of Oceanography, University of Washington, Seattle, Washington, USA.

Corresponding Author: D. P. Nicholson, Marine Chemistry and Geochemistry Department, Woods Hole Oceanographic Institution, MS 25, 266 Woods Hole Rd., Woods Hole, MA 02543, USA. (dnicholson@whoi.edu)

0148-0227/12/2010JC006856

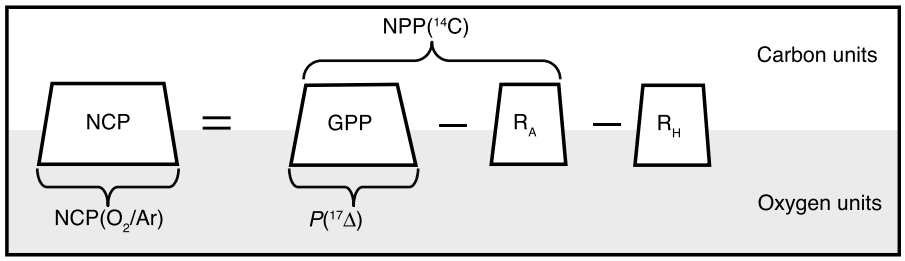

Figure 1. Schematic illustrating the relationships between different types of biological production and methods used for quantifying the rates of net community production (NCP), Gross primary production (GPP), net primary production (NPP), autotrophic respiration (R_A) and heterotrophic respiration (R_H). Rates are measured either in terms of production of oxygen, e.g., $P(^{17}\Delta)$) or production of organic carbon, e.g., (NPP(^{14}C)). Carbon and oxygen fluxes can be related by estimating the C:O_2 stoichiometry of each process.

record a more complete view of community metabolism than any one tracer alone. Comparing tracers that measure different aspects of community metabolism can lead to a better mechanistic understanding of ecosystem function and thus the prospect for better representation of ecosystems in models.

[4] Metabolism in an upper ocean marine ecosystem is composed predominantly from photosynthesis and respiration by autotrophs as well as respiration by heterotrophs and is often measured in terms of carbon fluxes [*Falkowski and Woodhead*, 1992]. Gross primary productivity (GPP) represents the total amount carbon dioxide that is photosynthetically reduced by autotrophs. Of gross carbon fixed, a portion is respired by autotrophs (R_A) during cellular metabolism [*Falkowski et al.*, 2003]. The difference between GPP and R_A is net primary production (NPP), or the amount of carbon made available to the heterotrophic community. The balance of whole ecosystem photosynthesis and respiration in the euphotic zone is termed net community production (NCP) and is the difference between NPP and heterotrophic respiration (R_H). NCP is the most important rate to the global carbon cycle, as it is a measure of the amount of carbon available for export via the biological pump. Respiration rates, R_A in particular, are very difficult to measure in the field, but in theory each of the five rates mentioned above can be determined by measuring GPP, NPP and NCP and calculating respiration rates by difference (Figure 1).

[5] In this paper, we investigate how GPP is calculated from observations of triple oxygen isotopes, and how such GPP estimates compare to traditional ^{14}C productivity incubations, which most closely represent NPP over the course of 12 to 24 h incubation studies [*Bender et al.*, 1987; *Marra*, 2009]. We focus on two data-rich locations, the BATS and HOT stations, and interpret recent triple oxygen isotope time series measurements [*Luz and Barkan*, 2000, 2009; *Quay et al.*, 2010] by adding oxygen isotopes to a one-dimensional mixed layer model. Studies have widely used observed triple oxygen isotopes to infer mixed layer GPP assuming steady state mixed layer conditions, with little ability to test the amount of error introduced by such assumptions. By combining observations with modeling, we quantify the degree to which entrainment and non steady state mixed layer dynamics may bias estimates of GPP calculated from mixed-layer field observations.

1.1. Tracers of Primary Productivity

1.1.1. ^{14}C Incubation Measure of NPP

[6] The in vitro ^{14}C incubation method of estimating NPP (NPP(^{14}C)) was originally introduced by *Steemann Nielsen* [1952] and has become one of the most widely measured biological properties made at sea. In the ^{14}C method radiocarbon labeled dissolved inorganic carbon (DI^{14}C) is added to incubation experiments. After a period of time (12 or 24 h), the water sample is filtered and the incorporation of ^{14}C into particulate organic matter is quantified.

[7] The ^{14}C method has a number of limitations and potential sources of bias. A primary and inherent concern with the method is the impact of bottle effects, caused by incubation of a relatively small volume of water that potentially could have altered conditions of community structure, trace metal abundance, and grazing in addition to lacking physical mixing and turbulence of the in situ environment [*Harrison and Harris*, 1986; *Marra*, 2002; *Peterson*, 1980]. The dynamic irradiance conditions of the in situ environment are also not reproduced in an incubation study. Additional concerns relate to the use of ^{14}C as a marker of carbon uptake. During incubation, recycling of labeled ^{14}C as well as exudation of ^{14}C as dissolved organic carbon (DO^{14}C) lower estimated primary productivity [*Harrison and Harris*, 1986; *Peterson*, 1980]. Such issues may cause NPP(^{14}C) to overestimate or underestimate true NPP [*Bender et al.*, 1987, 1999; *Luz et al.*, 2002]. Another challenge is that the ^{14}C method measures NPP on a spatial scale of a sampling bottle and on a daily temporal scale. Such discrete measurements present a challenge when scaling up to large spatial and temporal domains. Despite the caveats, recent syntheses have argued that NPP(^{14}C) can reasonably represent NPP in the ocean [*Marra*, 2009].

1.1.2. Triple Oxygen Isotope Tracer of *P*

[8] To assess GPP, we focus on the triple oxygen isotope method [*Luz and Barkan*, 2000]. Because oxygen is measured, the triple oxygen isotope method records gross oxygen production (P) rather than GPP. The two rates are closely linked by the C:O stoichiometry of photosynthesis. Dissolved oxygen in the ocean has two primary sources: (1) atmospheric oxygen that enters the water through air-sea gas exchange and (2) photosynthetically produced oxygen, created from the oxidation of seawater. Precise measurements of the natural abundance of stable oxygen isotopes

(^{16}O, ^{17}O, ^{18}O) in dissolved oxygen can be used to assess GPP because these two sources of oxygen in seawater have distinct isotopic signatures [*Luz and Barkan*, 2000; *Luz et al.*, 1999]. The oxygen isotopic composition of tropospheric O_2 is distinct due to reactions in the stratosphere involving O_2, O_3, and CO_2 that cause a non mass-dependent fractionation effect, creating an anomalously low $\delta^{17}O$ relative to $\delta^{18}O$ [*Lämmerzahl et al.*, 2002; *Luz et al.*, 1999; *Thiemens et al.*, 1995]. The excess (or deficit) of ^{17}O relative to ^{18}O ($^{17}\Delta$) is defined in relation to a reference standard and a reference slope (λ) as [*Angert et al.*, 2003; *Luz and Barkan*, 2005]

$$^{17}\Delta = \ln\left(1+\delta^{17}O\right) - \lambda \ln\left(1+\delta^{18}O\right), \quad (1)$$

where $^{17}\Delta$ is reported in per meg for clarity by multiplying by 10^6 and the isotopic abundance, δ*O is calculated from the isotopic ratio of sample relative to the ratio of a standard using delta notation ($\delta^*O = R_s/^*R_{ref} - 1$) where '*' denotes $^{17}O/^{16}O$ or $^{18}O/^{16}O$ ratio and R_s and R_{ref} are the isotopic ratio of the sample and reference gas (air O_2), respectively. For describing the dissolved ^{17}O excess we adopt a reference slope of $\lambda = \gamma_R = 0.518$ following *Luz and Barkan* [2005]. The value γ_R is the ratio of isotopic fractionation during respiration ($\gamma_R = {}^{17}\varepsilon_R/{}^{18}\varepsilon_R$) and was determined from the trend line of $\ln(1+\delta^{17}O)$ versus $\ln(1+\delta^{18}O)$ due to one-way, mass dependent process of ordinary respiration and was demonstrated to be applicable for respiration for a wide range of organisms [*Luz and Barkan*, 2005]. Because ordinary respiration is the most widespread O_2 consuming mechanism on Earth, *Luz and Barkan* [2005] suggested using this value for calculating ^{17}O-excess in the dissolved oxygen. In this case respiratory fractionation alone changes both $\delta^{17}O$ and $\delta^{18}O$, but does not alter $^{17}\Delta$ (for more details see *Luz and Barkan* [2009]).

[9] In equation (1), $^{17}\Delta$ of air O_2 is zero by definition since air is the chosen primary reference gas. A small equilibrium isotope effect results in the $^{17}\Delta$ of seawater dissolved oxygen in equilibrium with the atmosphere ($^{17}\Delta_{eq}$) to be slightly higher than zero, ranging from 4 to 17 per meg over the water temperature range of 3.5–25°C [*Luz and Barkan*, 2009; *Stanley et al.*, 2010]. We choose to apply the temperature dependent relationship of *Luz and Barkan* [2009]. Photosynthetically produced O_2 (directly produced by photosynthetic oxidation of VSMOW water molecules) has been recently estimated to be $\delta^{17}O_P = -20.014‰$ and $\delta^{18}O_P = 0.236‰$ [*Barkan and Luz*, 2011]. These values correspond to a biological equilibrium end-member ($P = R$ steady state) of $\delta^{17}O_{bio} = -0.014‰$, $\delta^{18}O_{bio} = -10.126‰$ and $^{17}\Delta_{bio} = 244$ per meg [*Angert et al.*, 2003; *Kaiser and Abe*, 2011; *Kaiser*, 2011; *Luz and Barkan*, 2011; *Nicholson*, 2011]). This recently determined end-member is very similar to the original biological end-member of $^{17}\Delta_{bio} = 249 \pm 15$ per meg [*Barkan and Luz*, 2011; *Luz and Barkan*, 2000]. The observed $^{17}\Delta$ of dissolved oxygen in seawater ($^{17}\Delta_{dis}$) thus should fall between the two end-members, $^{17}\Delta_{eq}$ (~16 per meg) and $^{17}\Delta_{bio}$ (244 per meg), at a value determined by the relative proportion of dissolved oxygen originating from the atmosphere versus photosynthesis. Of importance is the fact that $^{17}\Delta_{dis}$ is primarily altered by gas exchange and photosynthesis and not respiration. $^{17}\Delta_{dis}$ is defined such that respiration acting alone does not alter $^{17}\Delta_{dis}$ (for more details see *Luz and Barkan* [2009]). Thus for any observed $^{17}\Delta_{dis}$, if the residence time of dissolved oxygen with respect to gas exchange is known, a rate of photosynthetic oxygen production can be calculated by mass balance.

[10] We note that there is some debate as to the appropriate value for each end-member, $^{17}\Delta_{eq}$ and $^{17}\Delta_{bio}$ [*Kaiser*, 2011; *Prokopenko et al.*, 2011; *Stanley et al.*, 2010]. Either a lower $^{17}\Delta_{eq}$ or lower $^{17}\Delta_{bio}$ value both would increase the P calculated from any given measured $^{17}\Delta_{dis}$ value, as the observation would be closer to the biological end-member. *Luz and Barkan* [2011] found species specific variability in $^{17}\Delta_{bio}$ of about ±20 per meg. Community shifts could therefore cause modest biases in P calculated from ^{17}O excess. While future reevaluation/remeasurement of the gas exchange and biological end-members would shift the absolute values of our results somewhat, our main conclusions on the importance of biases introduced by entrainment and nonsteady state dynamics are robust.

[11] The gross rate at which O_2 is processed by photosynthesis (P) is stoichiometrically linked to the rate of carbon fixation (GPP) by the photosynthetic quotient (PQ) ratio [*Laws et al.*, 2000]. P and GPP can be decoupled, however, due to processes such as photorespiration and the Mehler reaction in which O_2 is processed in photosystem I with little or no reduction of CO_2 to organic C, processes that may be influenced by environmental conditions such as light and nutrient availability.

[12] The triple oxygen isotope method has been applied as a tracer of P in varied ocean environments, including the subtropics [*Juranek and Quay*, 2005; *Luz and Barkan*, 2000, 2009; *Quay et al.*, 2010], tropical Pacific [*Hendricks et al.*, 2005; *Stanley et al.*, 2010], coastal Japan [*Sarma et al.*, 2008, 2005] and Southern Ocean [*Hendricks et al.*, 2004; *Reuer et al.*, 2007]. Most of these studies have sought to use oxygen isotope measurements to constrain P in the mixed layer. Using a steady state mixed layer assumption and parameterizations of gas exchange rate, P integrated over the mixed layer has been approximated by the equation [*Luz and Barkan*, 2000]

$$P_{ml(SS)} \approx k_{O_2} O_{eq} \frac{{}^{17}\Delta_{dis} - {}^{17}\Delta_{eq}}{{}^{17}\Delta_{bio} - {}^{17}\Delta_{dis}}. \quad (2)$$

[13] $P_{ml(SS)}$ is mixed layer integrated P, k_{O2} is the air-sea gas transfer coefficient for O_2, and O_{eq} is the equilibrium solubility concentration [*García and Gordon*, 1992]. $^{17}\Delta_{bio}$, $^{17}\Delta_{dis}$, $^{17}\Delta_{eq}$ are the triple oxygen isotope anomalies of photosynthetically produced oxygen, dissolved oxygen, and oxygen from air-sea gas exchange, respectively. It is advisable to use a gas transfer coefficient, k_{wt}, that is weighted over the residence time of O_2 in the mixed layer [*Reuer et al.*, 2007]. The above equation assumes that the mixed layer is in steady state with respect to $[O_2]$. Thus dissolved oxygen with a composition of $^{17}\Delta_{dis}$ must be removed (by respiration and net outgassing) at the same rate as it is produced by P with a composition of $^{17}\Delta_{bio}$. In the above equation, approximations are made that ignore the slight dependences of the solution on $[O_2]/[O_2]_{eq}$ and δ*O, which can result in a small systematic bias in equation (2) [*Hendricks et al.*, 2004;

Kaiser, 2011; *Prokopenko et al.*, 2011]. To avoid this bias we apply a more rigorous derivation for all of our calculations [*Kaiser*, 2011; *Prokopenko et al.*, 2011]

$$P_{ml(SS)} = k_{wt} O_{eq} \frac{\left(1 - \frac{\delta^{17}O_{eq}+1}{\delta^{17}O_{dis}+1}\right) - \gamma_R\left(1 - \frac{\delta^{18}O_{eq}+1}{\delta^{18}O_{dis}+1}\right)}{\left(\frac{\delta^{17}O_{bio}+1}{\delta^{17}O_{dis}+1} - 1\right) - \gamma_R\left(\frac{\delta^{18}O_{bio}+1}{\delta^{18}O_{dis}+1} - 1\right)}. \quad (3)$$

[14] The above rigorous equation is still based on the assumption of a steady state mixed layer. In regions such as the subtropics, where $^{17}\Delta_{\mathrm{dis}}$ is elevated below the mixed layer, entrainment of $^{17}\Delta$ enriched water violates the steady state assumption and can lead to an overestimate of true mixed layer *P*. By 'entrainment' we refer to all physical processes transferring water between mixed layer and thermocline. At both BATS and HOT our results suggest that this flux is dominated by changes in mixed layer depth and associated entrainment and detrainment events, with diffusive mixing playing a much smaller role. Winter periods when the mixed layer is deep are also a concern because the residence time of O_2 with respect to gas exchange becomes many months and the mixed layer may not have time to reach a steady state. Because of such potential biases, the ability to estimate mixed layer *P* from surface observations alone has been limited to those times when entrainment bias is not expected to be large [*Luz and Barkan*, 2009; *Quay et al.*, 2010]. Later we evaluate the bias in mixed layer calculations induced by entrainment through the annual cycle at HOT and BATS.

[15] Equations (2) and (3) only consider *P* in a steady state mixed layer. Following the derivations of *Prokopenko et al.* [2011] and *Kaiser* [2011], an additional term can be added to correct for nonsteady state conditions ($P(z)_{(NSS)}$). This term can be applied across the whole euphotic zone depth and requires a time series of $^{17}\Delta$ observations made throughout the euphotic zone. To date, such measurements have only been made at two locations, BATS [*Luz and Barkan*, 2009] and HOT [*Quay et al.*, 2010]. $P(z)_{(NSS)}$ is estimated from the time rate of change of $^{17}\Delta$ such that

$$P(z)_{(NSS)} = O\left(\frac{(^{17}\Delta_{dis})_{t_2} - (^{17}\Delta_{dis})_{t_1}}{t_2 - t_1}\right) \Big/ \left(\left(\frac{\delta^{17}O_{bio}+1}{\delta^{17}O_{dis}+1} - 1\right) - \gamma_R\left(\frac{\delta^{18}O_{bio}+1}{\delta^{18}O_{dis}+1} - 1\right)\right), \quad (4)$$

where t_2 and t_1 are two measurement times. Note that $P(z)_{(NSS)}$ is the gross oxygen production rate at a fixed depth and not column integrated (i.e., mol m^{-3} s^{-1} rather than mol m^{-2} s^{-1}). δ^*O_{dis} is evaluated as the average of values at t_2 and t_1 and $^{17}\Delta_{\mathrm{dis}}$ values are a function of δ^*O_{dis} as described by equation (1). To get the euphotic zone integrated nonsteady state term ($P_{eu(NSS)}$), equation (4) can be integrated over a depth range using the trapezoid rule. In equation (4), if $^{17}\Delta_{\mathrm{dis}}$ is decreasing with time, $P(z)_{(NSS)}$ will be negative and correct the steady state term downward, and vice versa when $^{17}\Delta_{\mathrm{dis}}$ is increasing. Total euphotic zone *P* (P_{eu}) is approximated as the sum of $P(z)_{(NSS)}$ integrated from euphotic zone base to surface and P_{ml} from equation (3)

$$P_{eu} = P_{ml(SS)} + P_{eu(NSS)}. \quad (5)$$

1.1.3. Relating P to NPP

[16] When considering the difference between *P* and NPP, it is important to consider three types of biological processes: (1) Those that split water, producing oxygen without an associated reduction of CO_2, thus decoupling *P* and GPP; (2) variations in the photosynthetic quotient (PQ), which influence the C:O metabolic stoichiometry; and (3) variations in the fraction of GPP subject to autotrophic respiration, altering the *P*:NPP ratio.

[17] In the first category, pathways such as the Mehler reaction result in photosynthetic processing of O_2 that is not linked to carboxylation. Although no net oxygen is produced, the triple oxygen isotope method records Mehler reaction activity as *P* because it alters $^{17}\Delta_{\mathrm{dis}}$ [*Helman et al.*, 2005]. In the Mehler reaction water molecules are split in photosystem II producing O_2 with an isotopic signature of $^{17}\Delta_{\mathrm{bio}}$ but then subsequently different O_2 molecules, from the ambient O_2 pool with composition $^{17}\Delta_{\mathrm{dis}}$, are reduced in photosystem I [*Bender et al.*, 1999]. Mehler reaction activity is stimulated by light and its major physiological role is likely as a pathway for dissipating excess photon energy flux [*Badger et al.*, 2000]. Mehler reaction splitting of water has been assumed to account for roughly 15% of total *P* [*Bender et al.*, 1999; *Laws et al.*, 2000] but significant uncertainty exists. For example, *Trichodesmium* exhibit much higher Mehler reaction rates, with Mehler activity accounting for about half of total electron flow [*Kana*, 1993]. In *Trichodesmium* the Mehler cycle helps to preserve anaerobic microenvironments necessary for nitrogen fixation [*Berman-Frank et al.*, 2001]. Photorespiration results in binding of a portion of *P* by Rubisco, the resulting products of which largely are respired rather than used for cellular synthesis (GPP), but photorespiration is generally small in magnitude in marine autotrophs [*Laws et al.*, 2000]. The plastiquinol oxidase (PTOX) pathway also decouples photosynthetic activity from carbon fixation, serving as a mechanism for ATP creation while avoiding photoinhibition and photosystem damage [*Zehr and Kudela*, 2009].

[18] The PQ for oxygen production and carbon uptake depends on the redox state of the nitrogen substrate and is 1.1 for ammonia based productivity (recycled production), and 1.4 for nitrate based primary production (new production) [*Laws*, 1991]. Assuming 85% of primary production is recycled yields a PQ of 1.15. Because recycled production dominates over new production at both BATS and HOT, an assumed PQ ratio of 1.15 is likely accurate to within a few percent.

[19] Beyond variations in the O_2:C ratio of gross production, variations in the carbon use efficiency of primary producers alters the ratio of gross to net primary productivity (GPP:NPP). Variations in this ratio are due to variability in the fraction of gross carbon fixation allocated to autotrophic respiration. A more efficient allocation of fixed carbon to growth, rather than to metabolic maintenance, results in a lower *P*:NPP ratio.

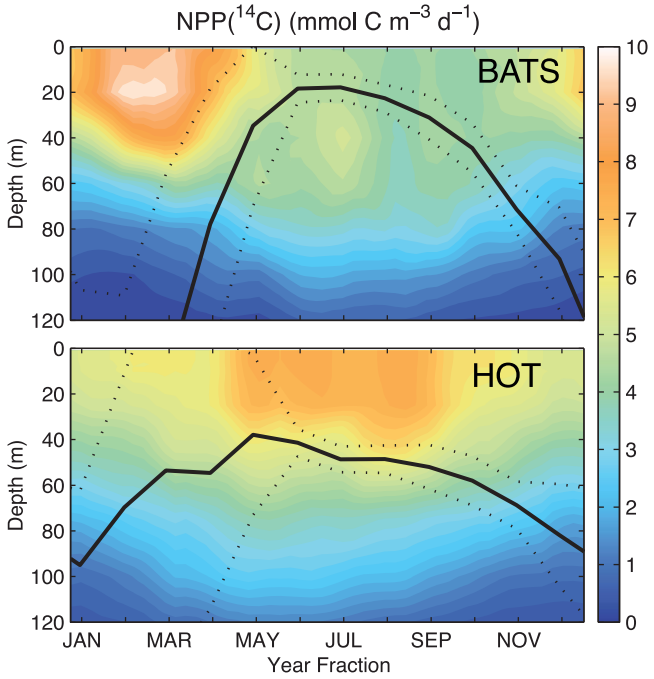

Figure 2. Annual composite of NPP(^{14}C) at (top) BATS and (bottom) HOT over ~20 years. Black lines represent monthly mean mixed layer depths averaged over all cruises. Dashed lines are standard deviation bounds for mixed layer depth of each month. Productivity at BATS is dominated by a late winter/early spring bloom that occurs as the water column stratifies. Greatest productivity at HOT is observed during episodic productivity bursts during the summer months. At BATS, the winter mixed layer is deeper than at HOT, but the summer mixed layer is shallower. More NPP (^{14}C) occurs below the shallow summer mixed layer at BATS than at HOT.

1.1.4. Previous Studies of Gross:Net Ratios

[20] The ratio of gross to net primary productivity is an important measure of the flow of energy through an ecosystem and of the efficiency of the autotrophic community in processing carbon. The gross to net ratio has previously been assessed by comparing ^{18}O incubation measurements of P ($P(^{18}O)$) and 24-h ^{14}C incubations for NPP [*Bender et al.*, 1999; *Marra*, 2002]. *Marra* [2002] compiled JGOFS data from the equatorial Pacific, subarctic North Atlantic and Arabian Sea to calculate a widely cited $P(^{18}O)$:NPP(^{14}C) ratio of 2.7 (mol O_2/mol C). Because $P(^{18}O)$ is also an incubation-based measurement, the technique determines P on the same instantaneous and local scale as does NPP (^{14}C). For 12-h ^{14}C incubations, the expected ratio is 2.0 [*Marra*, 2002; *Quay et al.*, 2010]. According to *Marra* [2009], daytime 12-h incubations most closely reproduce NPP, and are slightly higher than 24-h incubation results due to less recycling of ^{14}C.

[21] Studies at HOT that have included P from $^{17}\Delta$ ($P(^{17}\Delta)$) and $P(^{18}O)$ have found mixed layer $P(^{17}\Delta)$ to be significantly larger (25 to 73%) than concurrent $P(^{18}O)$ [*Juranek and Quay*, 2005; *Quay et al.*, 2010]. The difference was attributed to bottle effects for $P(^{18}O)$, entrainment effects and differences in integration time between the methods. The integration timescale of dissolved gas geochemical tracer methods (e.g., $^{17}\Delta$) is determined by the residence time of O_2 in the euphotic zone with respect to gas exchange, which ranges from days/weeks for the mixed layer (approximated by mixed layer depth divided by gas transfer velocity), to a season for the seasonal thermocline to many years for the permanently stratified thermocline [*Jenkins and Goldman*, 1985; *Spitzer and Jenkins*, 1989]. Because of the broader integration scale of the in situ geochemical tracers, episodic productivity events may be better captured by $P(^{17}\Delta)$, but missed by $P(^{18}O)$, which is a daily measurement. Comparison of $P(^{18}O)$ and NPP(^{14}C) productivity incubations at HOT showed a distinct trend with depth, linearly decreasing from 2.4 at the surface to 1.1 at 100 m [*Quay et al.*, 2010].

[22] $P(^{17}\Delta)$:NPP(^{14}C) results have generally exceeded the ratio of 2.7 of *Marra* [2002]. In a few locations, much higher P:NPP(^{14}C) ratios have been observed. At BATS [*Luz and Barkan*, 2009] and Lake Kinneret, Israel, [*Luz et al.*, 2002] report ratios as high as 7.9 and 7.6, respectively. Using $^{17}\Delta$ and a satellite based estimate of NPP, a ratio of 5.4 was inferred in the Southern Ocean [*Reuer et al.*, 2007]. In the Equatorial Pacific, $P(^{17}\Delta)$:NPP(^{14}C) was found to be high in the Western Equatorial Pacific (8.2 ± 4.0), but within error of 2.7 in the Central and Eastern Equatorial Pacific [*Stanley et al.*, 2010]. In the Celtic Sea, an average ratio of 4.5 was observed for $P(^{18}O)$:NPP(^{14}C) [*Robinson et al.*, 2009]. Some of these studies have found P:NPP(^{14}C) to be higher during bloom periods [*Luz and Barkan*, 2009; *Robinson et al.*, 2009].

1.2. Study Sites

[23] Full depth profiles of NPP(^{14}C) and $^{17}\Delta_{dis}$ have been measured simultaneously at two locations in the subtropics, the time series stations HOT (22°45′N, 158°W) and BATS (30°40′N, 64°10′W). Both time series programs routinely measure NPP(^{14}C) through the euphotic zone at roughly monthly intervals. The HOT program performs 12-h incubations, while BATS measures uptake over a 24-h period. $^{17}\Delta_{dis}$ was measured at HOT over a two-year period from 2006 to 2008 [*Quay et al.*, 2010]. At BATS, $^{17}\Delta_{dis}$ was measured from 1998 to 2003 [*Luz and Barkan*, 2000, 2009] (see Table S1).[1] BATS and HOT represent perhaps the two most studied sites in the ocean, with a wide range of biological, chemical and physical parameters measured over the last 20 years [*Karl and Lukas*, 1996; *Steinberg et al.*, 2001]. The richness of supporting data makes BATS and HOT ideal sites to compare and contrast the underlying mechanisms controlling various metabolic rates of their respective upper ocean ecosystems.

[24] Both locations are in subtropical gyres and thus have a number of fundamental similarities [*Ducklow et al.*, 2009; *Karl and Lukas*, 1996; *Michaels and Knap*, 1996; *Steinberg et al.*, 2001]. At both sites, Ekman convergence results in downwelling, very low biomass in surface waters and oligotrophic conditions. Also at both sites subsurface chlorophyll maxima are present, and a significant amount of primary productivity occurs below the mixed layer depth.

[25] Despite these similarities, striking differences in the seasonal pattern of primary productivity exist, as evident in an annual composite of the approximately 20 years of NPP (^{14}C) measurements at each site (Figure 2). At BATS, the

[1] Auxiliary materials are available in the HTML. doi:10.1029/2010JC006856.

highest productivity has long been recognized to occur in late winter/early spring and is associated with an annual bloom event [*Riley*, 1957; *Sverdrup*, 1953]. After the short duration, early spring bloom, highest levels of primary productivity are observed below the mixed layer during summer months. At HOT, highest primary productivity is observed during summer months in the mixed layer. Integrated primary productivity at HOT is about 15% higher in summer than in winter [*Karl and Lukas*, 1996]. From year to year, the highest annual productivity occurs in the mixed layer at varying times during the stratified summer season [*Ducklow et al.*, 2009; *Karl and Lukas*, 1996]. Significant and variable productivity also occurs below the mixed layer. Overall, there is less seasonal variability in primary productivity at HOT than at BATS.

[26] Primary productivity at HOT and BATS is intimately linked to the physical setting of each location. Mixed layer dynamics determine seasonal nutrient supply and set distinct biogeochemical regimes within and below the mixed layer. BATS is located in a region of large meridional gradients in many properties, including mixed layer depth [*Steinberg et al.*, 2001]. To the north, in mode water formation regions, deep mixing occurs to depths in excess of 300 m [*Marshall et al.*, 2009], providing a large supply of nutrients to surface waters each winter, and supporting nutrient replete conditions. To the south, shallower winter mixed layer depths are 100 m or less and more oligotrophic, subtropical conditions exist. BATS can experience significant interannual variability in mixed layer depth, with winter mixed layer depths ranging from 150 m to in excess of 300 m [*Doney*, 1996; *Steinberg et al.*, 2001]. Winter mixing at BATS is generally sufficiently deep to entrain nutrients needed to fuel a seasonal bloom. At HOT, winter mixing is shallower, most years reaching about 100 m and rarely penetrating the nutricline [*Karl and Lukas*, 1996]. During spring at both HOT and BATS the water column stratifies and mixed layer depth shoals. In the summer BATS mixed layer depth consistently shoals to shallower depths (~20 m) than at HOT (~40 m) (Figure 2).

2. Methods

2.1. $^{17}\Delta$ Data

[27] Triple oxygen isotope measurements were made on samples collected during BATS and HOT cruises using similar methodology. Data and methodology for observations from 1998 to 2000 at BATS have been published [*Luz and Barkan*, 2000, 2009]. In this paper, we report an additional two years (2001–2002) of previously unpublished measurements from Luz and Barkan (see Table S1). The two-year time series of observations at HOT was reported in *Quay et al.* [2010].

2.2. Physical Model

[28] We use a modified one-dimensional, vertical Price-Weller-Pinkel (PWP) model [*Price et al.*, 1986] to simulate the upper 1000 m at HOT and BATS (Table 1). The physical model is forced by diurnally varying, 6-hourly NCEP wind stress, heat flux and precipitation [*Kistler et al.*, 2001]. Following *Stanley et al.* [2006, 2009], vertical velocities associated with Ekman pumping were calculated from low-pass filtered wind stress curl and tapered to zero at the base of the model domain. To account for lateral heat imbalance and correct for any systematic error in NCEP heat flux, a horizontal heat flux offset was added (H_{off}). The magnitude of H_{off}, the depth over which the heat correction is distributed (Z_H), and the background vertical diffusivity (K_z) were each considered tunable model parameters. The model was run with a wide range of parameters to determine the ideal combination that minimized root mean squared (RMS) temperature anomaly when compared to time series observations at BATS and HOT. Best fit values were determined to be $H_{off} = -28$ W m^{-2}, $K_z = 9 \times 10^{-5}$ m^2 s^{-1} and $Z_H = 50$ m at BATS for the period 1997–2003 and $H_{off} = 12$ W m^{-2}, $K_z = 8 \times 10^{-5}$ m^2 s^{-1} and $Z_H = 200$ m at HOT for the period 2006–2008. RMS was 0.568°C at BATS and 0.294°C at HOT. After optimizing H_{off}, Z_H and K_z, the model temperature profile was relaxed to observed values with a time constant (τ) of 70 days. The physical model exhibits skill in reproducing mixed layer depth, sea surface temperature and heat content (Figure 3).

2.3. Oxygen Isotopes and Gases in the PWP Model

[29] Vertical 1-D mixed layer models have been extended to include the cycling of dissolved gases at both HOT [*Hamme and Emerson*, 2006] and BATS [*Spitzer and Jenkins*, 1989; *Stanley et al.*, 2006, 2009]. Here, we extend the model of *Stanley et al.* [2006, 2009] to include oxygen isotopes, ^{16}O, ^{17}O and ^{18}O, each explicitly represented in the model. Transport of each oxygen isotope is the same, but fractionation can occur during gas exchange at the air-sea interface and during biological processes. For all calculations, isotopic values are computed relative to air O_2 as the standard.

2.3.1. Air-Sea Fractionation

[30] QuikSCAT winds were used to calculate air-sea gas transfer velocities at both BATS and HOT. At both sites, 12-hourly QuikSCAT winds were better correlated with National Data Buoy Center (NDBC) wind speed measurements than were NCEP winds. Continuous NDBC mooring winds were not available for the entire period of model simulation. QuikSCAT winds were not available for the first 19 months at BATS, so NCEP winds were substituted, after correcting them based on a local linear regression between NCEP and QuikSCAT. This correction decreased NCEP winds at BATS by ~12%. Air-sea gas exchange in the model is parameterized following *Stanley et al.* [2009] as the sum of diffusive gas exchange (F_{ge}) fluxes and fluxes from completely (F_{bc}) and partially (F_{bp}) collapsing bubbles. Including bubble fluxes improves representation of oxygen saturation in the upper ocean but proved here to have a negligible impact on $^{17}\Delta$. Including bubbles results in a correction of less than 1 per meg. Air-sea fluxes of oxygen and oxygen isotopes are modeled so that the total air-sea flux of oxygen, F_{tot} is

$$F_{tot} = -k_{O_2}\left(O_{surf} - \frac{p_{slp}}{p_0} O_{eq}\right) + F_{bc} + F_{bp}, \qquad (6)$$

where k_{O2} is the gas piston velocity for oxygen, p_{slp} is sea level pressure in atmospheres, p_0 is the reference pressure of 1 atm, O_{surf} is the surface oxygen concentration and O_{eq} is the

Table 1. Selected Model Parameters Used for Simulations at BATS and HOT

Parameters	Abbreviation	Value		References[a]	Units
		BATS	HOT		
Model Parameters					
Lateral heat offset	H_{off}	−28	12		W m^{-2}
Depth range for H_{off}	Z_H	50	200		m
Vertical diffusivity	K_z	8.0×10^{-5}	$1.x \times 10^{-5}$		m^2 s^{-1}
Root mean squared temperature error	RMS_T	0.568	0.2935		°C
Temperature restoring constant	τ	70			d
QuikSCAT 10-m wind speed	u_{10}	variable			m s^{-1}
Air-sea gas flux	F	variable			mol m^{-2} s^{-1}
Gas transfer scaling factor (relative to *Wanninkhof* [1992])	γ_G	0.9332		1	–
Coefficient for complete bubble trapping	A_C	2.3×10^{-11}		1	s^2 m^2
Coefficient for partial bubble trapping	A_P	5.8×10^{-4}		1	s^2 m^2
Sea level pressure	p_{slp}	variable		atm	
Mass dependent slope for ordinary respiration	γ_P	0.518		2	1
Triple oxygen isotope ^{17}O excess	$^{17}\Delta$	$\ln(1+\delta^{17}O) - \lambda \ln(1+\delta^{17}O)$		2, 3	per meg
Equilibrium $^{17}\Delta$	$^{17}\Delta_{eq}$	$(0.6 \times T_{surf} + 1.8) \times 10^{-6}$ (T_{surf} in °C)		4	per meg
Biological steady state $^{17}\Delta$ end-member	$^{17}\Delta_{bio}$	244 per meg		3, 5, 6	per meg
Photosynthetic oxygen composition (versus air)	$\delta^{18}O_P$	−20.014‰		5	‰
Photosynthetic oxygen composition (versus air)	$\delta^{17}O_P$	−10.126‰		5	‰
Model Run Notation					
Gross O_2 production	P	Column integrated production			mol m^{-2} d^{-1}
	$P(z)$	Production at a given depth			mol m^{-3} d^{-1}
Equation used (subscript)	(*SS*)	Steady state P from equation (3)			–
	(*NSS*)	Nonsteady state P term from equation (4)			–
Depth range (subscript)	*eu*	Integrated to euphotic depth (140 m)			–
	ml	Integrated to mixed layer depth			–
Gross O_2 production type (superscript)	*INPUT*	P used to force model (based on NPP(^{14}C))			–
	MOD	Best fit model run			–
	NO_ENT	No entrainment model run			–
Fractionation Factors					
Equilibrium fractionation factor	$^{18}\alpha_{eq}$	$1 + (-0.73 + 427/T_K)/1000$ (T_K in K)		7	1
	$^{17}\alpha_{eq}$	$^{18}\alpha_{EQ}^{0.518} \times (\exp(^{17}\Delta_{EQ}))$		–	1
Gas exchange kinetic fractionation	$^{18}\alpha_{gek}$	0.9972		8	1
	$^{17}\alpha_{gek}$	$1 + \lambda\,(^{18}\alpha_{GEK} - 1) =$ 0.9985496		–	1
Respiration fractionation	$^{18}\alpha_R$	0.980		9	1
	$^{17}\alpha_R$	$1 + \gamma_P\,(^{18}\alpha_R - 1) = 0.98964$		3	1
Partial trapping bubble fractionation factor	$^{18}\alpha_{bp}$	$^{18}\alpha_{eq}\,(^{18}\alpha_{gek})^{2/3}$		1	1
	$^{17}\alpha_{bp}$	$^{17}\alpha_{eq}\,(^{17}\alpha_{gek})^{2/3}$		1	1

[a]References: 1, *Stanley et al.* [2009]; 2, *Luz and Barkan* [2005]; 3, *Angert et al.* [2003]; 4, *Luz and Barkan* [2009]; 5, *Luz and Barkan* [2011]; 6, *Barkan and Luz* [2011]; 7, *Benson and Krause* [1980]; 8, *Knox et al.* [1992]; 9, *Guy et al.* [1993].

equilibrium oxygen concentration at p_0 for surface temperature (T) and salinity (S) conditions. Gas piston velocity, k_{O2}, was calculated as quadratic function of QuikSCAT wind speed squared and scaled proportionally to Schmidt number to the −1/2 power [*Stanley et al.*, 2009]. This parameterization is based on constraints from a time series of noble gases measured at BATS, is specifically tuned for QuikSCAT winds [*Stanley et al.*, 2009]. The diffusive component of this parameterization results in gas transfer coefficients ∼7% lower than those from of *Wanninkhof* [1992], but roughly 20% higher than from other recent parameterizations [*Ho et al.*, 2006; *Nightingale et al.*, 2000; *Sweeney et al.*, 2007] each of which do not include an explicit bubble component.

The flux of ^{18}O (F_{tot}^{18}) is calculated by accounting for fractionation relative to the ^{16}O flux so that

$$F_{tot}^{18} = -{}^{18}\alpha_{gek} k_{O_2} \left({}^{18}r_{surf} O_{surf} - \frac{p_{slp}}{p_0} {}^{18}\alpha_{eq} {}^{18}r_{atm} O_{eq} \right) + {}^{18}r_{atm} F_{bc} + \alpha_{bp} {}^{18}r_{atm} F_{bp}, \quad (7)$$

where $^{18}\alpha_{gek}$ is the kinetic fraction factor during gas exchange, $^{18}\alpha_{eq}$ is the equilibrium fractionation factor, and $^{18}\alpha_{bp}$ is the fractionation factor due to partial trapping of bubbles [*Stanley et al.*, 2009]. ^{18}r is the ^{18}O/^{16}O isotope ratio, with the subscripts *surf* and *atm* referring to dissolved O_2 in

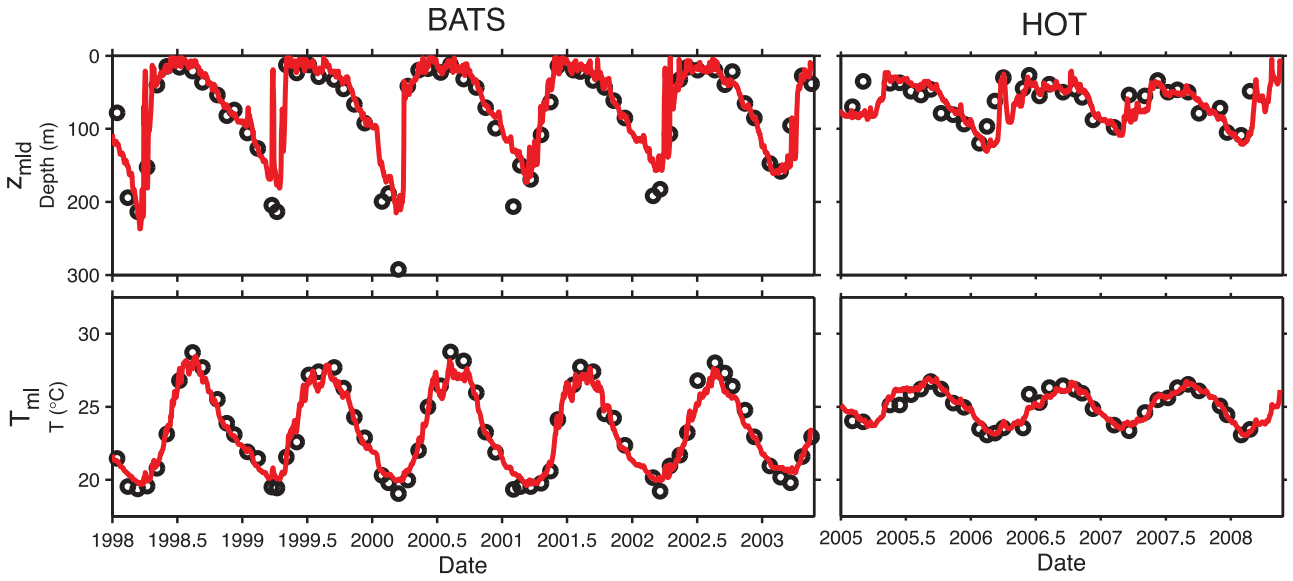

Figure 3. Physical model performance for (left) BATS and (right) HOT for (top) mixed layer depth and (bottom) mixed layer temperature. Red lines are model simulation and black circles are observations.

surface water and atmospheric oxygen, respectively. The equation for the air-sea flux of ^{17}O is analogous to that for ^{18}O.

[31] For the kinetic gas exchange fraction, we use values of $^{18}\alpha_{gek} = 0.9972$ [*Knox et al.*, 1992] and $(^{17}\alpha_{gek} - 1) = 0.518(^{18}\alpha_{gek} - 1)$. Air-sea equilibrium fractionation for $^{18}O/^{16}O$ is a function of water temperature where $^{18}\alpha_{eq} = 1+(-0.73 + 427/T_K)/1000$ where T_K is temperature in kelvin [*Benson and Krause*, 1980, 1984]. To account for the atmospheric equilibrium oxygen isotope anomaly, $^{17}\Delta_{eq}$, air-sea fractionation for ^{17}O is set so that

$$^{17}\alpha_{eq} = {}^{18}\alpha_{eq}^{0.518} \times \left(1 + {}^{17}\Delta_{eq}\right) \text{ where } {}^{17}\Delta_{eq} = 0.6 \times T_{surf} + 1.8, \quad (8)$$

as determined by *Luz and Barkan* [2009], where T_{surf} is surface temperature in °C. No fractionation occurs for completely collapsing bubbles, since their entire contents are injected in atmospheric ratio. For partially collapsing bubbles, bubble flux is proportional to the product of solubility and diffusivity to the 2/3 power ($\beta D^{2/3} \propto \beta k^{1/3}$) and thus $^*\alpha_{bp} = {}^*\alpha_{eq}\ ({}^*\alpha_{gek})^{1/3}$. Since the contribution of partially trapped bubble injection flux is relatively small, bubbles had a negligible effect on $^{17}\Delta_{dis}$.

2.3.2. Biological Fractionation

[32] The time rate of change of oxygen due to biology can be described as the balance between gross photosynthetic oxygen production (P) and total consumption of oxygen by respiration (R) where $R > 0$

$$\frac{\partial O}{\partial t} = P - R. \quad (9)$$

[33] For ^{18}O, a similar equation can be written with fractionation of biological sources and sinks

$$\frac{\partial^* O}{\partial t} = P^* r_P - R^* \alpha_R{}^* r_{dis}, \quad (10)$$

where '*' refers to either 18 or 17 and $^*r_P$ is the $^*O/^{16}O$ ratio of photosythetically produced O_2 and $^*\alpha_R$ is the fractionation factor during respiration. Fractionation of $\delta^{18}O$ and $\delta^{17}O$ during photosynthesis is small but can vary slightly depending on species [*Eisenstadt et al.*, 2010; *Guy et al.*, 1993]. In the model we use the estimated mean value for a range of photoautotrophs of $\delta^{18}O_P = -20.014‰$ and $\delta^{17}O_P = -10.126‰$ [*Barkan and Luz*, 2011]. Thus in the model during photosynthesis, oxygen is added with a $\delta^{18}O_P$ relative to air of −20.014‰, slightly enriched from the composition of seawater ($\delta^{18}O_{vsmow} = -23.324‰$, ($\delta^{17}O_{vsmow} = -11.883‰$ [*Barkan and Luz*, 2011]). Respiration causes a mass dependent fractionation relative to the ratio of dissolved oxygen; the fractionation factor is variable, but in marine organisms has been determined to be about −20‰ [*Kiddon et al.*, 1993] ($^{18}\varepsilon_R = -20‰$ ($^{18}\alpha_R = 0.980$), $^{17}\varepsilon_R = \gamma_P^{18}\varepsilon_R = -10.36‰$ ($^{17}\alpha_R = 0.98964$)). Setting $\delta^{17}O_P$ and $\delta^{18}O_P$ to values derived from experiments conducted using seawater of VSMOW composition does not capture the variations in seawater $\delta^{18}O$ due to evaporation/precipitation and biology observed in the real ocean [*Levine et al.*, 2009; *Luz and Barkan*, 2010], but these processes should have negligible influence on the ^{17}O excess biological end-member, $^{17}\Delta_{bio}$. Model parameters are summarized in Table 1.

2.4. Biology in the PWP Model

[34] To determine best fit rates of photosynthesis necessary to drive biological fractionation of O_2, BATS and HOT NPP (^{14}C) measurements were interpolated to the model domain and multiplied by a time-invariant P:NPP(^{14}C) ratio. Initial P:NPP(^{14}C) ratios were set based on an a priori value based on the literature, then adjusted to determine the ratio that best reproduced observed triple oxygen isotope anomalies. Fitting model results to $^{17}\Delta_{dis}$ in this manner provides the optimal P rates for each site without introducing potential sources of bias (such as entrainment) that would occur when applying equations (2) and (3).

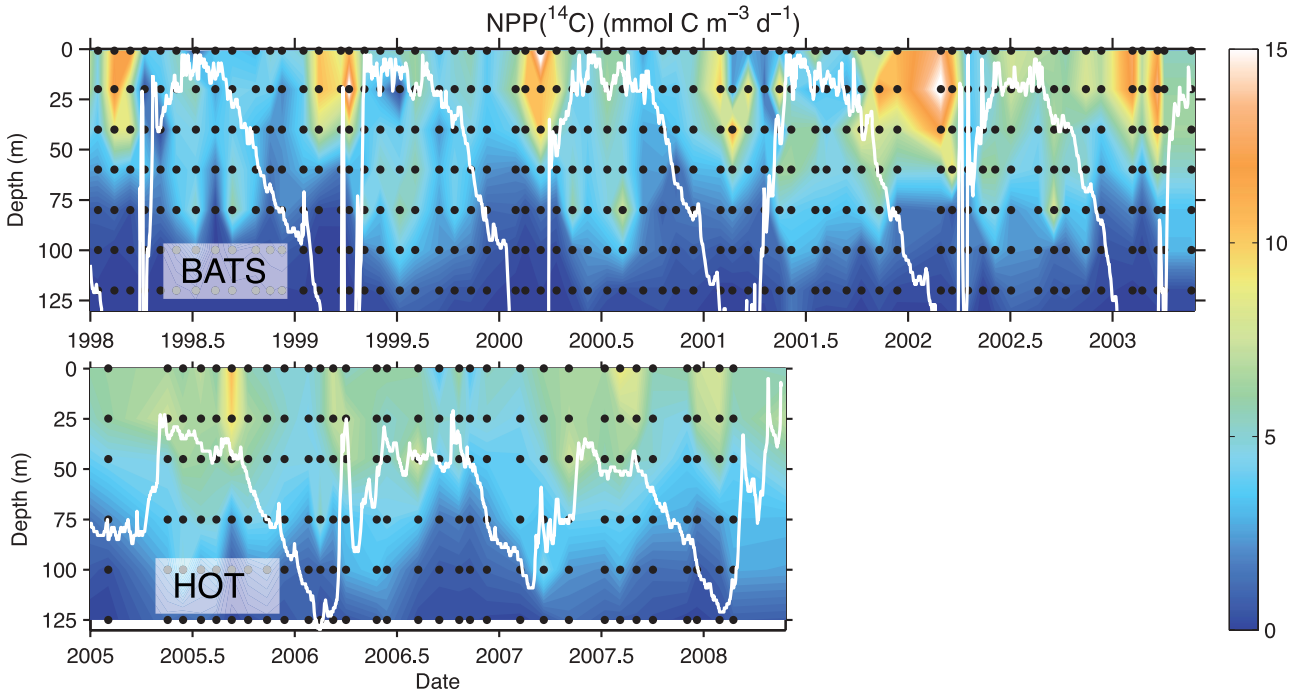

Figure 4. Time series of measured NPP(^{14}C) (mmol C m^{-3} d^{-1}) values linearly interpolated to model grid at (top) BATS and (bottom) HOT. Black dots show time and depth of measurements. White lines are model mixed layer depth using a $\sigma_\theta = 0.125$ kg m^{-3} cutoff criteria.

[35] By comparing results from JGOFS ^{18}O incubation studies for P and 24-h ^{14}C productivity incubations, *Marra* [2002] determined a P:NPP ratio of 2.7 (mmol O_2 m^{-3} d^{-1}/ mmol C m^{-3} d^{-1}). More recently, *Quay et al.* [2010] found the best fit $P(^{18}O)$:NPP(^{14}C) ratio at HOT to linearly decrease from 2.4 at the surface to 1.1 at 100 m. Therefore our a priori prediction is that $P = 2.7 \times$ NPP(^{14}C) at BATS while at HOT, a priori P was set by multiplying ^{14}C by the depth dependent ratio from *Quay et al.* [2010]. The model was then run at each site with a range of P:NPP(^{14}C) ratios varying from 1.0 to 5.0 to determine the ratio that would best reproduce observed values. The depth dependent ratio at HOT was adjusted by multiplying the whole profile by a constant. For example, when P was 4.8 at the surface, it decreased linearly to 2.2 at 100 m. For HOT, both the depth dependent ratio and a constant depth ratio were tested. In the time dimension, NPP (^{14}C) was linearly interpolated between ~monthly sampling times.

[36] NCP in the model was set using an idealized productivity curve from surface to compensation depth, with respiration below set in proportion to oxygen utilization rate (OUR) such that depth-integrated NCP was zero following *Stanley et al.* [2009]. The magnitude of euphotic zone NCP of O_2 was seasonally modulated following a sine curve peaking in June with an annual magnitude of 2.5 mol m^{-2} y^{-1} typical of subtropical rates of NCP [*Gruber et al.*, 1998; *Stanley*, 2007]. While the NCP parameterization influenced the net oxygen evolution in the model, it had only as small impact on $^{17}\Delta_{dis}$ because $^{17}\Delta_{dis}$ is not directly affected by respiration and is only weakly sensitive to changes in NCP. The effect of the magnitude of NCP is shown in the auxiliary material. Doubling NCP was found to increase $^{17}\Delta_{dis}$ by less than 2 per meg, an amount smaller than the analytical uncertainty of the measurements. Our calculated $^{17}\Delta_{dis}$ and conclusions about P were therefore insensitive to the assumed NCP parameterization.

3. Results

3.1. Model Results

[37] At BATS, the model was run from 13 January 1997 to 31 May 2003 and at HOT, was run from 21 December 2004 to May 2008. At each site, the model was initialized using hydrographic data from BATS and HOT observations. NPP (^{14}C) rates which were used to determine model $P(z)$ were linearly interpolated (first in depth, then in time) from BATS and HOT data (Figure 4). The seasonal pattern of productivity during the study period was similar to that observed in climatology (Figure 2) but with significant year-to-year variability. At BATS, highest NPP(^{14}C) was observed during the late winter/early spring bloom each year. A secondary, sub-mixed layer productivity maximum was also evident each year at BATS. NPP(^{14}C) at HOT had less seasonality than at BATS, and tended to have both higher and deeper productivity during summer rather than in winter.

[38] Root mean squared (RMS) error between $^{17}\Delta_{dis}$ model output and observations was determined for model runs with P:NPP(^{14}C) ratios varying from 1.0 to 5.0. RMS was normalized so that the mixed layer and sub-mixed layer data were weighted equally. At BATS, the best fit was P:NPP (^{14}C) = 2.6 (+0.9 −0.8). The same procedure was used for HOT, except that depth dependent P:NPP(^{14}C) ratios were used. The best fit ratio for both mixed layer and thermocline was P:NPP(^{14}C) = 3.0 (+1.0 −0.8) at the surface, declining to 1.4 (+0.6 −0.6) at 100 m (Figure 5). Error estimates are the 95% confidence interval assuming squared error between

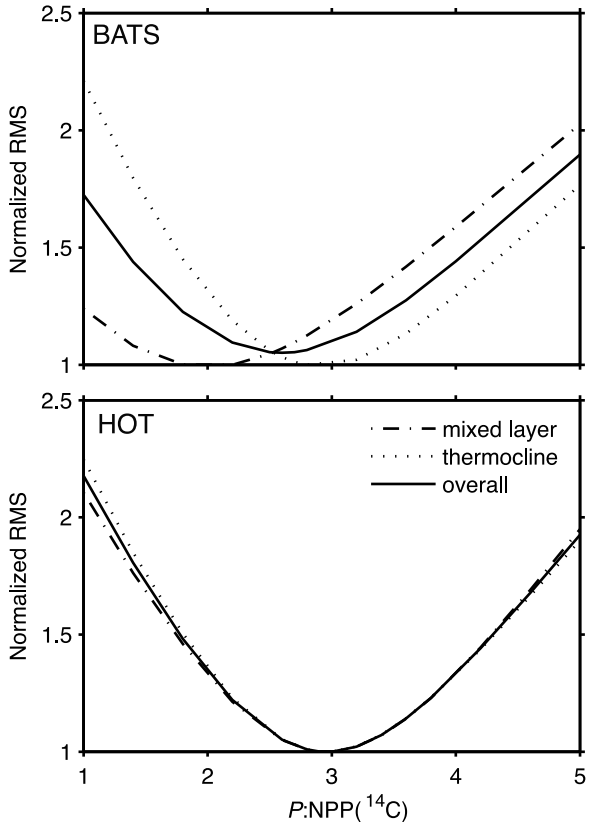

Figure 5. Root mean squared error (RMS) between observed $^{17}\Delta_{dis}$ and model simulations with a range of *P*:NPP(^{14}C) ratios. (top) For BATS, the *P*:NPP(^{14}C) of each simulation was constant with depth while (bottom) for HOT, the *x* axis represents the surface ratio. The overall ratio at HOT decreased linearly with depth such that *P*:NPP(^{14}C) at 100 m was 1.1/2.4 times the surface value [*Quay et al.*, 2010]. RMS was normalized to make the minimum RMS equal to one for mixed layer and thermocline so that averaging the two would give each equal weighting in determining the overall fit.

observations and model has a χ^2 distribution (and thus asymmetric error bounds) with the degrees of freedom estimated as one each for mixed layer and sub-mixed layer for each monthly profile of observations.

[39] Using the best fit *P*:NPP(^{14}C) relationships to determine model *P*, the time-dependent evolution of $^{17}\Delta_{dis}$ was simulated at BATS and HOT (Figure 6). The best fit simulation does an overall good job of reproducing observations in both the mixed layer (Figure 7a) and below (Figure 7b). Mixed layer observations at BATS did show some temporal variability not captured by our model, but no clear annual cycle was evident in optimal *P*:NPP(^{14}C). Sustained *P*:NPP (^{14}C) above 5.0 was not observed at either BATS or HOT. In the thermocline, the seasonal peak in $^{17}\Delta_{dis}$ at BATS exceeded the best fit simulation in each of the first three years of observations, approaching the *P*:NPP = 5.0 result (Figure 7), but not in the final year. At HOT, the best fit model result generally matches observations more consistently through the year.

[40] We thus determine the optimal *P* rate in the model by directly comparing NPP(^{14}C) to $^{17}\Delta_{dis}$ observations. The best fit *P*:NPP(^{14}C) ratios represent our best estimate of true *P* rates and *P*:NPP ratios at BATS and HOT. Furthermore, our results do not invoke equations (2) or (3) and thus are free from the steady state assumptions inherent to these equations. The model best fit *P* depends on model physics and biological and air-sea exchange equations (7) and (9). We refer to the photosynthetic rates from optimal model fits as $P(z)^{INPUT}$.

3.2. Mixed Layer *P*

[41] Our best fit model runs provide a test of how well equation (3) performs within an internally consistent model framework. The 'true' P_{ml} rates used to force the optimal model runs (P_{ml}^{INPUT}) are prescribed and can be directly compared to the P_{ml} calculated from the steady state equation (3) and model output fields of $\delta^{18}O_{dis}$ and $\delta^{17}O_{dis}$ (we refer to this *P* rate as $P_{ml(SS)}^{MOD}$). Note that while $P(z)^{INPUT}$ is interpolated from near-monthly ^{14}C observations, the mixed layer integrated value, P_{ml}^{INPUT}, varies on much shorter time scales, as it is integrated to the model mixed layer depth, which changes rapidly (Figure 8). The difference between P_{ml}^{INPUT} and $P_{ml(SS)}^{MOD}$ is introduced by the assumptions of steady state inherent to equation (3) that do not hold in our model or in the real world.

[42] For the mixed layer, $P_{ml(SS)}^{MOD}$ always exceeded P_{ml}^{INPUT} at both HOT and BATS (Figure 8). The reason for the overestimation is due primarily to entrainment of high $^{17}\Delta_{dis}$ water from below and to errors due to the time-lag in reaching a steady state mixed layer after changes in mixed layer depth (Figure 8). Entrainment results in ^{17}O excess originally produced below the mixed layer to be 'counted' as mixed layer production. Equation (3) assumes both a constant mixed layer depth, and no flux from below into the mixed layer. To remove the influence of both of these potential sources of error, an additional model sensitivity experiment was run for each study site. This additional experiment was forced with the same P_{ml}^{INPUT}, but to cancel the influence of entrainment, at each model time step ^{17}O concentrations at all depths below the mixed layer were reset so that $^{17}\Delta_{dis}$ was equal to the mixed layer ^{17}O excess such that entrainment events did not alter mixed layer $^{17}\Delta_{dis}$ (blue curve in Figure 8). We term this experiment NO_ENT. $P_{ml(SS)}^{NO\_ENT}$ is the *P* rate calculated from equation (3) and output fields of the NO_ENT experiment. The entrainment bias in the model is thus the difference between $P_{ml(SS)}^{MOD}$ and $P_{ml(SS)}^{NO\_ENT}$ (red – blue in Figure 8). *P* calculated from the NO_ENT experiment matched P_{ml}^{INPUT} well, demonstrating that equation (3) would be reasonably accurate if not for the effects of entrainment.

[43] The entrainment bias varied seasonally and was significant through the year. Even when there is no net deepening of the mixed layer, entrainment/detrainment events result in a flux across the mixed layer interface. At both BATS and HOT, entrainment was largest in late fall as the water column destratifies, and smallest in the spring as the water column stratifies (Figure 2). At BATS, the entrainment bias averaged 0.0239 ($\pm$0.006) mol O_2 m^{-2} d^{-1} in the spring (Apr–May–June) and 0.0647 ($\pm$0.015) mol O_2 m^{-2} d^{-1} in the fall (Sept–Oct–Nov), while at HOT the bias was 0.0604 ($\pm$0.006) mol O_2 m^{-2} d^{-1} in the spring and 0.0562 mol (+0.010 −0.007) O_2 m^{-2} d^{-1} in the fall. Error ranges are based on uncertainty in the best fit *P*:NPP ratio as described in section 3.1. As a percentage of P_{ml}^{INPUT}, at BATS the bias in spring added an additional 72% to $P_{ml(SS)}^{MOD}$ relative to

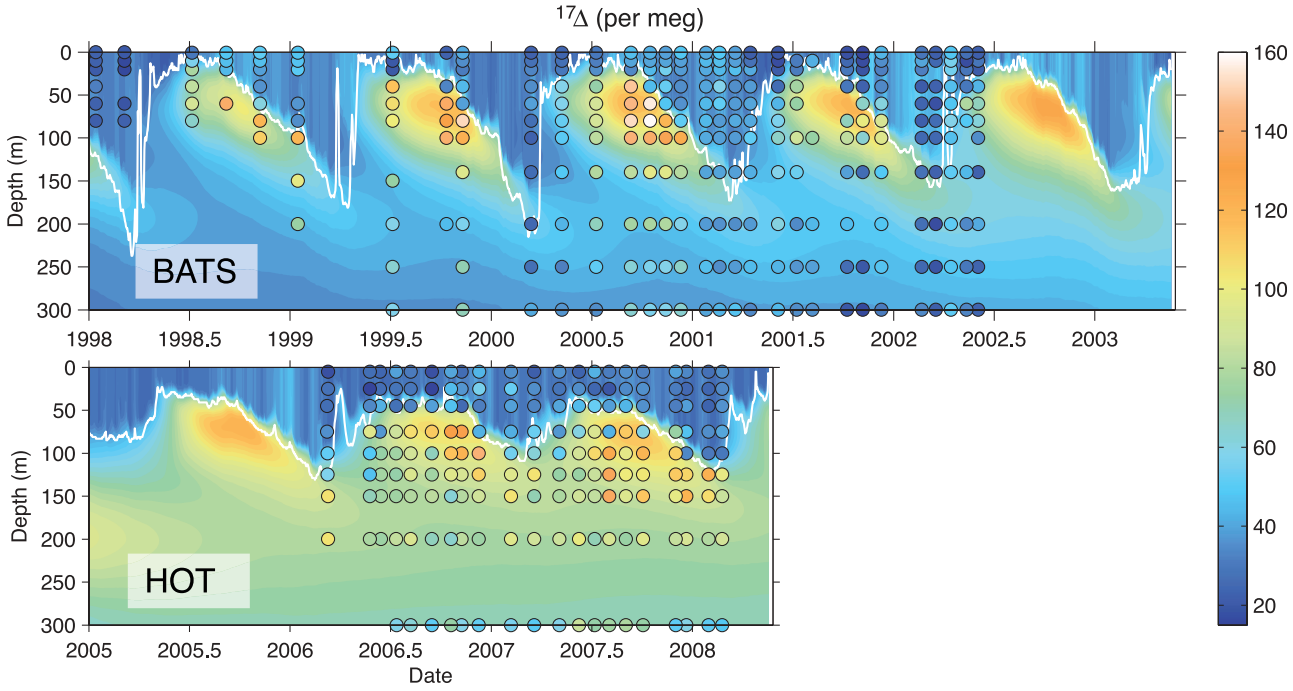

Figure 6. Measured and simulated $^{17}\Delta$ (per meg) at (top) BATS and (bottom) HOT using base case P:NPP(^{14}C) ratios of 2.6 at BATS and a ratio decreasing from 3.0 at the surface to 1.4 at 100 m for HOT. Circles are measured values, and colored field is model results. White lines are model mixed layer depth using $\Delta\sigma_\theta = 0.125$ kg m^{-3} cutoff criteria.

mixed layer $P_{ml(\overline{SS})}^{NO\_ENT}$ while the fall bias in $P_{ml(SS)}$ was 130% of fall $P_{ml(\overline{SS})}^{NO\_ENT}$. At HOT, the bias in the spring was 52% and in fall was 93%. Over the whole simulation period, entrainment bias was 81% of $P_{ml(\overline{SS})}^{NO\_ENT}$ at BATS and 63% of $P_{ml(\overline{SS})}^{NO\_ENT}$ at HOT.

[44] When mixed layer $P_{ml(SS)}^{MOD}$ and $P_{ml(\overline{SS})}^{NO\_ENT}$ are regressed against P_{ml}^{INPUT}, $P_{ml(\overline{SS})}^{NO\_ENT}$ falls near the 1:1 line as would be predicted. $P_{ml(SS)}^{MOD}$ shows a significant positive bias (above 1:1) that is evidence of the entrainment effect (Figure 9). P calculated from the mixed layer field observations and equation (3) ($P_{ml(SS)}^{OBS}$) in general matches $P_{ml(SS)}^{MOD}$ well, suggesting that the entrainment bias is in fact present in observations as well as in the model simulation. This implies that a model calculated entrainment bias (i.e., $P_{ml(SS)}^{MOD} - P_{ml(\overline{SS})}^{NO\_ENT}$) could be subtracted from observations ($P_{ml(SS)}^{OBS}$) to improve estimates of mixed layer production.

[45] The absolute values of $P_{ml(SS)}^{MOD}$ and $P_{ml(\overline{SS})}^{NO\_ENT}$ are sensitive to the choice of end-member parameters $^{17}\Delta_{bio}$ and $^{17}\Delta_{eq}$ but the relative magnitude of the entrainment value is not. For example, running the model with an alternate $^{17}\Delta_{bio}$ of 200 per meg means a higher P:NPP(^{14}C) ratio is necessary to match observations (3.3 at BATS and 3.8 to 1.7 at HOT). The resulting P_{ml}^{INPUT}, $P_{ml(\overline{SS})}^{NO\_ENT}$, $P_{ml(SS)}^{MOD}$ and absolute entrainment bias are similarly about 30% higher, but as a percentage of P, entrainment biases remained almost unchanged (annually, 80% at BATS and 63% at HOT).

3.3. Euphotic Zone Integrated *P*

[46] Averaged over the entire annual cycle $P_{ml(SS)}^{MOD}$ estimates annual total euphotic zone productivity well, because almost all of annually produced ^{17}O excess is eventually entrained and outgassed. However, $P_{ml(SS)}^{MOD}$ seasonally misattributes integrated P, overestimating in fall and underestimating at other times (Figure 10). To better capture seasonal variability, the nonsteady state term must be considered (equations (4) and (5)). P integrated over the depth of the euphotic zone (P_{eu}) can be calculated from a time series of $^{17}\Delta_{dis}$ through the euphotic zone (to 140 m) from equations (4) and (5) [*Kaiser*, 2011; *Luz and Barkan*, 2009; *Prokopenko et al.*, 2011; *Quay et al.*, 2010]. P_{eu} was calculated both from the time series of both modeled (P_{eu}^{MOD}) and measured (P_{eu}^{OBS}) $\delta^{18}O_{dis}$ and $\delta^{17}O_{dis}$ (Figure 10). During fall entrainment, $P_{eu(NSS)}^{MOD}$ becomes negative as column averaged $^{17}\Delta_{dis}$ is reduced, at the same time as $P_{ml(SS)}$ overestimates true P_{ml}. These two effects largely cancel in practice, although they are not mathematically equivalent. P_{eu}^{OBS} calculations should thus be used with caution and the accuracy of this approach will vary with the specific dynamics of any study location.

[47] For BATS and HOT we test the skill of the P_{eu} approximation by comparing P_{eu}^{MOD} calculated from model $\delta^{18}O_{dis}$ and $\delta^{17}O_{dis}$ to P_{eu}^{INPUT} used to force the model. One challenge of using equation (3) is that $P_{ml(SS)}$ provides a value integrated over the mixed layer gas residence time (weeks), while the depth integration calculation captures change that is averaged over the time between profiles (about month for data, but sub-daily for the model). When these two results are added together to calculate total P_{eu}^{MOD}, high frequency noise is introduced to the time series of integrated P_{eu}^{MOD} mainly due to high frequency variability in wind speed and mixed layer depth. To remove the high frequency component, a low-pass Butterworth filter (1/30 d^{-1} cutoff) was used before assessing P_{eu}^{MOD}. At both BATS and HOT, P_{eu}^{MOD} compared

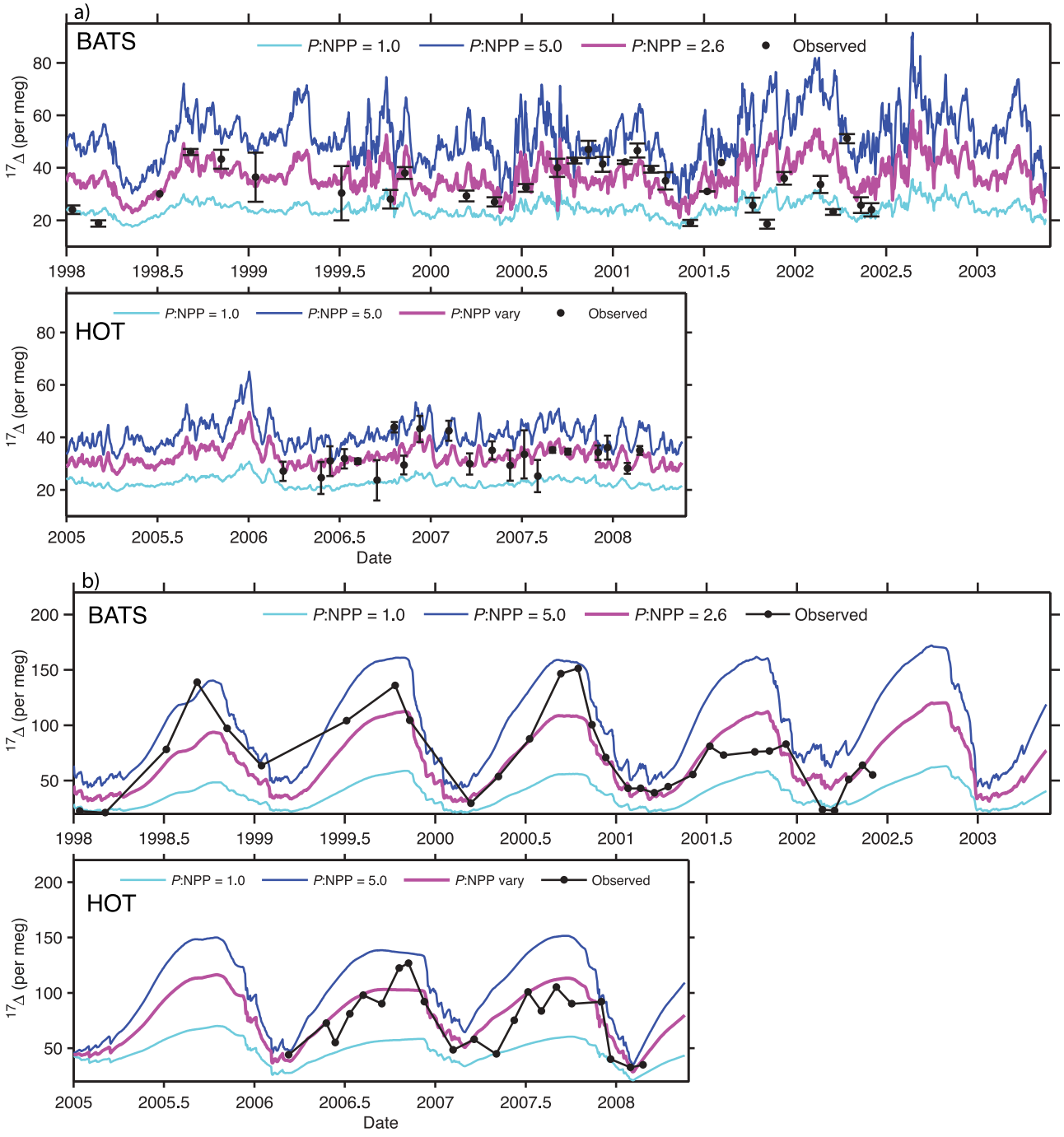

Figure 7. Simulated $^{17}\Delta_{dis}$ based on a *P*:NPP(^{14}C) (mmol O_2/mmol C) ratio of 2.6 (best fit case, magenta), 5.0 (high *P*, blue) and 1.0 (low *P*, cyan) for BATS and depth dependent ratio of 3.0–1.4 (best fit case, magenta), constant ratio of 5.0 (high *P*, blue) and 1.0 for HOT (low *P*, cyan). Black symbols are observed values. Error bars are the standard error of mixed layer measurements. (a) Mixed layer results and (b) mean 60–100 m results are shown.

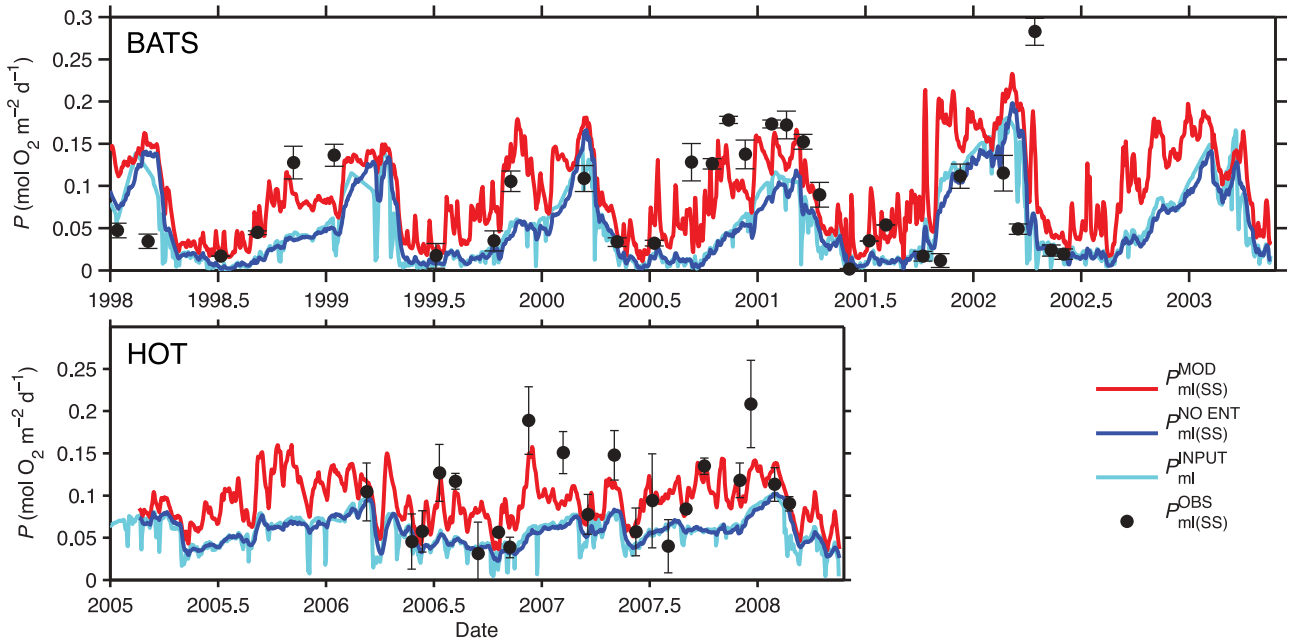

Figure 8. Mixed layer P calculated using equation (3) and model $\delta^{18}O_{dis}$ and $\delta^{17}O_{dis}$ ($P^{MOD}_{ml(SS)}$) is shown in red. Mixed layer P calculated with no flux from below ($P^{NO\_ENT}_{ml(SS)}$) is shown in blue. Black circles are P calculated from observed $\delta^{18}O_{dis}$ and $\delta^{17}O_{dis}$ values ($P^{OBS}_{ml(SS)}$). Error bars show standard error of the mean of mixed layer observations. Cyan lines are the model input P (P^{INPUT}_{ml}) calculated from NPP(^{14}C). The difference between the red and blue lines is the entrainment bias effect. The difference between the blue and cyan lines is mainly due to violation of the steady state assumption.

fairly well with the P^{INPUT}_{eu} derived from ^{14}C (Figure 10). P^{OBS}_{eu} was calculated from observations, excluding the first year at BATS when the full euphotic zone was not sampled. P^{INPUT}_{eu} was generally well reproduced when calculated from both model and observed $\delta^{18}O_{dis}$ and $\delta^{17}O_{dis}$. At both HOT and BATS, $P^{MOD}_{ml(SS)}$ and P^{MOD}_{eu} had similar average P to P^{INPUT}_{eu} but P^{MOD}_{eu} performed much better in capturing the seasonal cycles at these subtropical locations (Figure 10).

4. Discussion

4.1. Model Performance

[48] Overall at HOT P:NPP(^{14}C) exceeded the expected ratio (2.4 at surface, decreasing to 1.1 for 12-h incubations) by about 25%. Both mixed layer and thermocline observations were best reproduced with a depth dependent P:NPP (^{14}C) that decreased from 3.0 to 1.4 at 100 m. At BATS, the ratio of 2.6 relative to 24-h incubations provided the best fit to observations. However, the magnitude of the observed sub-mixed layer $^{17}\Delta_{dis}$ maximum in the summer exceeded model results in the best fit P:NPP(^{14}C) simulation for 1998–2000. To reproduce the high $^{17}\Delta_{dis}$ observations, in the 1-D model, a higher P:NPP(^{14}C) ratio must be invoked. No reasonable adjustment of model parameters such as diffusivity or Ekman pumping can be used to match the high thermocline $^{17}\Delta_{dis}$ observations. Thus, our a priori constant relationship between P and NPP appears to break down in the sub-mixed layer euphotic zone at BATS. Our 1-D model, however, cannot evaluate the possible role of lateral advection and mixing which may influence the thermocline $^{17}\Delta_{dis}$ budget. Global modeling of $^{17}\Delta_{dis}$ is needed to better evaluate the role of lateral transport for oxygen isotope budgets.

[49] In the mixed layer at BATS, the best fit model run (P:NPP(^{14}C) = 2.6) underestimates mixed layer $^{17}\Delta$ during summer/fall 1998 and overestimates it in winter 2001 and spring 2002. The error in the mixed layer $^{17}\Delta_{dis}$ may stem from misestimating $^{17}\Delta_{dis}$ of underlying water that is seasonally entrained, rather than any error in P in the mixed layer itself. The difference between mixed layer simulated and observed $^{17}\Delta_{dis}$ values corresponds to the observed mismatch in the sub-mixed layer. When the model subsurface maximum underestimated observed thermocline $^{17}\Delta_{dis}$ (e.g., 1998), simulated mixed layer $^{17}\Delta_{dis}$ was lower than the observed levels during the entrainment period. Conversely, in 2001 when the model subsurface maximum overestimated observed $^{17}\Delta_{dis}$, the model overestimates observed mixed layer values.

4.2. Inferring P From $^{17}\Delta_{dis}$

[50] When calculating P from $\delta^{18}O_{dis}$ and $\delta^{17}O_{dis}$, three physical environments should be considered: the mixed layer, the seasonal thermocline and the permanent thermocline. Depending on location and season, the euphotic zone could be limited to the mixed layer or extend below to include part of the seasonal or permanent thermocline. P influences $^{17}\Delta_{dis}$ in a distinctly different manner and on varying timescales for each zone. The isotopic composition of oxygen in the mixed layer is primarily a balance between gas exchange and P that occurs on a timescale of weeks. The accumulation of $^{17}\Delta_{dis}$ in the seasonal thermocline records an integrated measure of P from the time of spring stratification to the time of measurement. The $^{17}\Delta_{dis}$ in the permanent thermocline is best described as a balance between regional circulation including lateral ventilation processes

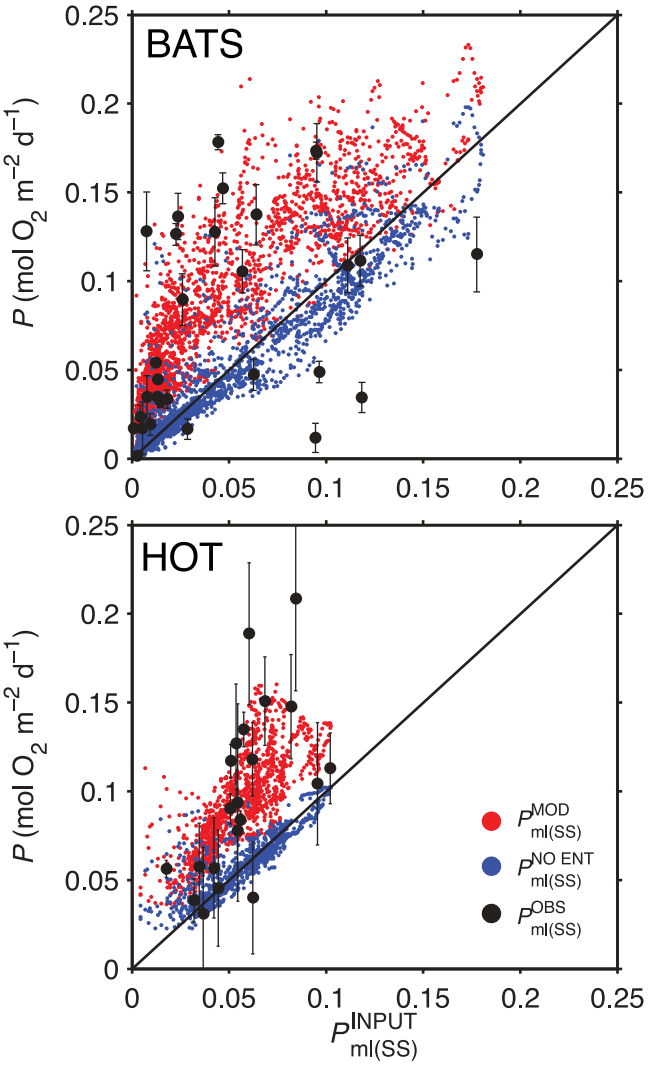

Figure 9. Mixed layer P calculated from simulated mixed layer $\delta^{18}O_{dis}$ and $\delta^{17}O_{dis}$ ($P^{MOD}_{ml(SS)}$) in red and mixed layer P calculated from no entrainment runs ($P^{NO\_ENT}_{ml(SS)}$) (blue) are plotted against P^{INPUT}_{ml}. P calculated from observations ($P^{OBS}_{ml(SS)}$) are compared to P^{INPUT}_{ml} using black dots. A 1:1 line is shown in black. Red dots falling above the 1:1 line indicates an entrainment bias in $P_{ml(SS)}$. Many observations appear to include a similar entrainment bias to that in model results.

and P and as such should not be interpreted in a 1-D framework. For example, the tropics tend to have shallow mixed layer depths and high light conditions, resulting in a sizable portion of the euphotic zone permanently residing below the mixed layer depth. The shifting boundaries between these three regimes can lead to challenges in interpretation.

4.2.1. Mixed Layer

[51] Mixed layer P calculated from equation (3) and compared to NPP(^{14}C) can lead to falsely high estimated P:NPP due to the entrainment of high $^{17}\Delta$ water from below the mixed layer. In the subtropical and tropical oceans, where the euphotic zone depth exceeds the mixed layer depth, a large subsurface $^{17}\Delta_{dis}$ signal develops and can be seasonally entrained into the mixed layer, raising mixed layer $^{17}\Delta_{dis}$. The potential for entrainment events to result in spuriously high mixed layer P has been well acknowledged [*Juranek and Quay*, 2005; *Luz and Barkan*, 2009; *Quay et al.*, 2010; *Sarma et al.*, 2005] however its magnitude is difficult to quantify. At HOT, Quay et al. estimated that entrainment bias was about 10% of P during summer and roughly 70% in winter, while *Sarma et al.* [2005] estimated a 15% overestimate in summer in Sagami Bay, Japan. Our modeling effort allows us to directly assess the magnitude and extent of the entrainment bias within the dynamically consistent framework of the model. In our model, entrainment caused a significant positive bias in P_{ml} through almost the entire year at both BATS and HOT, annually averaging to about 60 to 80% of mixed layer P. The bias was particularly large during the fall at both HOT and BATS since mixed layer depths were increasing. In the stratified summer, when mixed layers become very shallow, entrainment/mixing also was important. Our results suggest that when summer mixed layer P is low, even a small entrainment flux of $^{17}\Delta_{dis}$ during the spring-summer period causes the bias to be a large fraction of P_{ml} and thus is significantly more important than previous studies have estimated.

[52] Other processes that could violate the mixed layer steady state assumption, such as wind speed variations and mixed layer shoaling, cause relatively less bias at both BATS and HOT. When the entrainment flux was removed, $P^{NO\_ENT}_{ml}$ matched P^{INPUT}_{ml} well through most of the year. During the winter at BATS, when the mixed layer gets very deep, mixed layer $^{17}\Delta_{dis}$ does not have time to fully equilibrate with the atmosphere and could thus overestimate P (Figure 8). The entrainment bias should be considered the dominant source of error in calculating mixed layer P at BATS and HOT.

4.2.2. Thermocline

[53] A time series of $^{17}\Delta_{dis}$ observations can be used to calculate a vertically integrated P rate based on the time rate of change of $^{17}\Delta_{dis}$ using equation (5). Integrating over the full euphotic zone allows the overestimation in the mixed layer (from entrainment) to largely be balanced by the time rate of change of average $^{17}\Delta_{dis}$ of the water column, as deeper water is ventilated and high $^{17}\Delta_{dis}$ lost to the atmosphere. Using equation (5) and observations requires that the "spot" measurements of mixed layer $^{17}\Delta_{dis}$ derived air-sea flux are assumed to be constant over the duration between sampling (near-monthly). Because mixed layer $^{17}\Delta_{dis}$ and gas transfer rate are actually quite variable, significant error is introduced into the calculation of P_{eu} calculated over a short duration. The integrated method should therefore only be applied on seasonal to annual (or longer) time-scales [*Quay et al.*, 2010].

[54] Due to the role that physical dynamics plays in introducing biases into estimates of P, information on recent mixed layer and wind history is needed to gain insight on the accuracy of $^{17}\Delta_{dis}$ based P estimates. Single mixed layer measurements of $^{17}\Delta_{dis}$ should be interpreted with caution. A time series of profile measurements can provide the averaging needed to more accurately assess P. If mixed layer and wind speed history are known, a single profile of $^{17}\Delta_{dis}$ may be sufficient to back-calculate the effect of entrainment bias.

4.3. Implications at HOT and BATS

[55] The $^{17}\Delta$ dynamics at HOT and BATS are at first glance quite similar, with each developing a subsurface

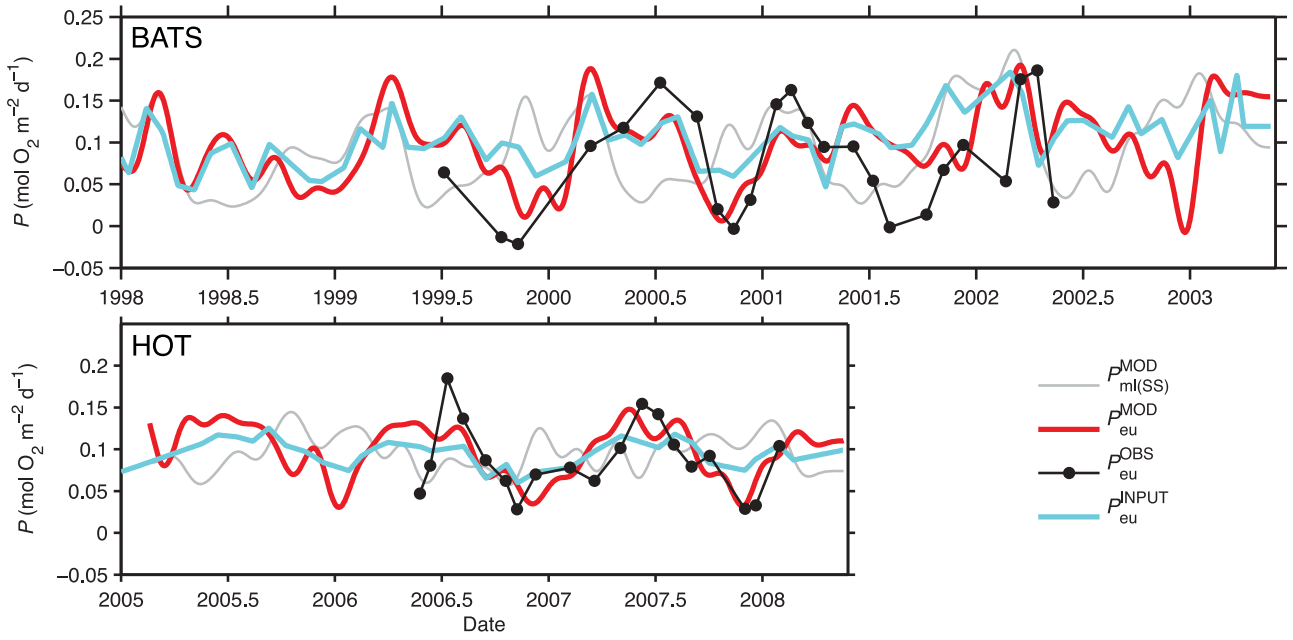

Figure 10. Model input depth-integrated P_{eu}^{INPUT} (cyan) from 0 to 140 m compared to integrated P_{eu}^{MOD} (red) and P_{eu}^{OBS} calculated from observations and equation (5) (black). The bold red P_{eu}^{MOD} line is filtered with a low-pass Butterworth filter with a 1/30 day cutoff frequency. Low-pass filtered $P_{ml(SS)}^{MOD}$ is shown in gray for comparison. Results (top) for BATS and (bottom) for HOT below are shown. Both model and data are overall in good agreement with P_{eu}^{INPUT}. Low-pass filtered $P_{ml(SS)}^{MOD}$ has a similar annual average to P_{eu}^{INPUT}, but does not track the seasonal cycle well.

maximum in $^{17}\Delta_{dis}$ in the seasonal thermocline reaching a maximum in the range of 100–150 per meg. Mixed layer values at both locations generally range from about 20–50 per meg. In the mixed layer, however, BATS has far greater seasonality, with $^{17}\Delta_{dis}$ peaking in early spring each year.

[56] Despite similarities in $^{17}\Delta_{dis}$, differences in the physical and biological environment at BATS and HOT results in significantly different interpretations. Mixed layer depth in summer at BATS are shallower than at HOT, which causes even small entrainment events to increase mixed layer $^{17}\Delta_{dis}$, resulting in a large bias in P relative to true mixed layer P. At HOT observations show that $^{17}\Delta_{dis}$ below the euphotic zone (150–200 m) is higher than at BATS. Winter mixing at BATS is significantly deeper than the euphotic zone depth causing the entire euphotic zone to be 'reset' each season. At HOT, winter mixed layer depth is generally shallower than the maximum depth of photosynthesis, allowing for incomplete equilibration of the deep euphotic zone with the atmosphere. In the deepest parts of the euphotic zone at HOT $^{17}\Delta_{dis}$ must be controlled by a balance between biological production and advective and mixing fluxes of $^{17}\Delta_{dis}$ on a multiyear timescale. At BATS, the entire euphotic zone $^{17}\Delta_{dis}$ is effectively reset each winter by gas exchange. This distinction is likely why higher and less variable $^{17}\Delta_{dis}$ is maintained at depth at HOT.

4.4. *P*:NPP

[57] The average *P*:NPP ratio of 2.7 determined from field incubation studies [*Marra*, 2002] ($P(^{18}O)$:NPP(^{14}C)) is similar to laboratory determined chlorophyll specific *P*:NPP rates of 3.3 for the chlorophyte *Dunaliella tertiolecta* [*Halsey et al.*, 2010]. *Halsey et al.* [2010] found that *P*:NPP rates were constant over a range of growth rates under nitrogen-limited, light saturated balanced growth conditions. A primary goal of our modeling effort was to reconcile the apparently higher $P(^{17}\Delta)$:NPP(^{14}C) from triple oxygen isotope field studies with laboratory and incubation based findings. Our results suggest that in some situations, biases in the triple isotope method can lead to a conclusion of falsely high *P*:NPP due to physical processes including the mixed layer entrainment bias we have described. In other regions, however, such as the deep euphotic zone at BATS, high *P*:NPP determined from $^{17}\Delta_{dis}$ and NPP(^{14}C) [*Luz and Barkan*, 2009] appear to be robust. Our conclusions are somewhat in contradiction to previous results, which have suggested high *P*:NPP ratios when productivity is high during bloom periods [*Luz and Barkan*, 2009; *Robinson et al.*, 2009] and generally high *P*:NPP(^{14}C) ratios often exceeding 5 [*Juranek and Quay*, 2010; *Quay et al.*, 2010; *Reuer et al.*, 2007]. After subtracting the entrainment bias at BATS and HOT, we found no correlation between mixed layer *P*:NPP(^{14}C) ratio and the magnitude of mixed layer NPP(^{14}C).

[58] At BATS, while some variability was evident, over the course of the study period the expected *P*: NPP(^{14}C) of 2.7 proved the best fit to observations. At HOT, the $^{17}\Delta_{dis}$ simulations are in good agreement with the observed decrease of *P*:NPP with increasing depth found in ^{18}O incubation data [*Quay et al.*, 2010] as well as in fast repetition rate fluorometry [*Corno et al.*, 2006]. By combining observed profiles with our model interpretation, we find that $^{17}\Delta_{dis}$ provide additional support for a depth dependent *P*:NPP(^{14}C) ratio as previously observed at HOT. However, *P* from $^{17}\Delta_{dis}$

was about 25% higher than calculated from ^{18}O incubations. That $P(^{17}\Delta_{dis})$ was higher than $P(^{18}O)$ is not entirely surprising, as the offset was previously observed by *Juranek and Quay* [2005] and *Quay et al.* [2010]. The surface *P*:NPP of 3.0 we estimate is also close to the value of 3.3 reported by *Halsey et al.* [2010], although Halsey *et al.* did not determine the effect of light limited growth on the *P*:NPP ratio. A decreasing activity of alternative electron pathways such as the Mehler reaction would provide a physiological explanation for the depth trend in *P*:NPP observed at HOT.

[59] Below the mixed layer at BATS, our combined observation and modeling interpretation is consistent with a high *P*:NPP(^{14}C) ratio of approximately five or greater, in agreement with the range of 3–5 reported by *Luz and Barkan* [2009] although a large lateral flux of $^{17}\Delta_{dis}$ could also be responsible for the observed elevated magnitude and seasonality of $^{17}\Delta_{dis}$. Our 1-D modeling framework does not account for the role of lateral advection and thus cannot distinguish between potential biological versus physical causes of the high $P(^{17}\Delta)$:NPP(^{14}C) in the deep euphotic zone. If local biological processes are responsible, high *P*:NPP ratios could be characteristic of the community of low light and nutrient adapted autotrophs that inhabit the seasonal thermocline. *Prochlorococcus* spp. is the numerically dominant member of the phytoplankton community in this zone [*DuRand et al.*, 2001] and potentially could have high autotrophic respiration and/or high Mehler cycle activity causing a decoupling between *P* and GPP. A physiological motivation for either is not obvious. The possibility that lateral advective processes play a role in increasing thermocline $^{17}\Delta_{dis}$ cannot be discounted. Future work will include 3-D modeling of triple oxygen isotopes to quantify lateral fluxes and analysis of $^{17}\Delta_{dis}$ profiles along sections. Another possible contributor to the high observed *P*:NPP values is that NPP(^{14}C) could underestimate true NPP. For example, a significant portion of ^{14}C uptake is exuded as $DO^{14}C$ [*Karl et al.*, 1998]. Further understanding how primary producers and environmental conditions influence the allocation of photosynthetic products will be essential to predicting how changing ecosystems will modify the bulk flow of nutrients and energy in the upper ocean.

5. Conclusions

[60] All tracers of primary productivity have their unique caveats and biases. Particularly when attempting to compare tracers that use different techniques, such as triple oxygen isotopes and ^{14}C incubations, care must be taken to account for the impact of such biases on interpretations. The modeling framework we apply allows for a more complete understanding of the $^{17}\Delta_{dis}$ data sets at BATS and HOT. The observed dynamics can be applied to gain insight into how the $^{17}\Delta_{dis}$ tracer will perform across varying bio-physical settings. In particular, the model results reveal that entrainment processes lead the steady state approach of equations (2) and (3) to significantly overestimate mixed layer *P* through most of the year (by 60–80%, annually averaged) in the subtropics due to underestimation of the entrainment bias. Averaged annually, the steady state approach yielded rates closer to full euphotic zone *P* rather than mixed layer *P*. Because deep euphotic zone *P* is only 'counted' when it is entrained, seasonal patterns in $P^{MOD}_{ml(SS)}$ can be severely biased by entrainment (Figure 10). Future global modeling of triple oxygen isotopes could identify regions where lateral transport, entrainment and/or upwelling cause either positive or negative biases in the $^{17}\Delta_{dis}$ tracer method.

[61] At HOT, we demonstrate that a large portion of the discrepancy between mixed layer $P(^{17}\Delta)$ relative to mixed layer $P(^{18}O)$ observed by *Quay et al.* [2010] was due to entrainment bias. After correcting for the entrainment bias, mixed layer *P* from $^{17}\Delta$ is about three times greater than NPP(^{14}C) and about 25% greater than $P(^{18}O)$. Our model $^{17}\Delta_{dis}$ simulations support a *P*:NPP(^{14}C) ratio that decreases with depth, just as was observed from in the $P(^{18}O)$ record. The consistency between the two fundamentally different *P* tracer techniques ($^{17}\Delta_{dis}$ and ^{18}O) suggest that there exists a variation in the *P*:NPP(^{14}C) ratio due either to systematic biases in ^{14}C incubations or to systematic changes in ecosystem metabolism with depth. At BATS, mixed layer $P(^{17}\Delta)$ calculated from a steady state mixed layer assumption (equations (2) and (3)) has led to high inferred *P*:NPP values of 3–8 in the autumn [*Luz and Barkan*, 2009]. Our model results suggest that physical biases rather than biological variation may be the dominant cause of the high mixed layer ratios reported at BATS. Below the mixed layer at BATS, either a very high *P*:NPP ratio or lateral advective processes likely are responsible for the seasonal summer peak in $^{17}\Delta_{dis}$ observed most years. Model simulations demonstrate that the details of the physical system, and the potential for biases must be considered in addition to biological effects when seeking to interpret mixed layer $^{17}\Delta_{dis}$.

[62] **Acknowledgments.** We acknowledge support from Center for Microbial Oceanography Research and Education (CMORE) (NSF EF-0424599) and NOAA Global Carbon Program (NA 100AR4310093) and thank Maria Prokopenko and an anonymous reviewer for their helpful comments. BL thanks the USA-Israel Binational Science Foundation for supporting his project at BATS.

References

Angert, A., S. Rachmilevitch, E. Barkan, and B. Luz (2003), Effects of photorespiration, the cytochrome pathway, and the alternative pathway on the triple isotopic composition of atmospheric O_2, *Global Biogeochem. Cycles*, *17*(1), 1030, doi:10.1029/2002GB001933.

Badger, M. R., S. von Caemmerer, S. Ruuska, and H. Nakano (2000), Electron flow to oxygen in higher plants and algae: Rates and control of direct photoreduction (Mehler reaction) and rubisco oxygenase, *Philos. Trans. R. Soc. London, Ser. B*, *355*(1402), 1433–1446, doi:10.1098/rstb.2000.0704.

Barkan, E., and B. Luz (2011), The relationships among the three stable isotopes of oxygen in air, seawater and marine photosynthesis, *Rapid Commun. Mass Spectrom.*, *25*(16), 2367–2369, doi:10.1002/rcm.5125.

Bender, M., et al. (1987), A comparison of four methods for determining planktonic community production, *Limnol. Oceanogr.*, *32*(5), 1085–1098, doi:10.4319/lo.1987.32.5.1085.

Bender, M., J. Orchardo, M.-L. Dickson, R. Barber, and S. Lindley (1999), In vitro O_2 fluxes compared with ^{14}C production and other rate terms during the JGOFS Equatorial Pacific experiment, *Deep Sea Res., Part I*, *46*(4), 637–654, doi:10.1016/S0967-0637(98)00080-6.

Benson, B. B., and D. Krause (1980), The concentration and isotopic fractionation of gases dissolved in freshwater in equilibrium with the atmosphere. Part 1. Oxygen, *Limnol. Oceanogr.*, *25*(4), 662–671, doi:10.4319/lo.1980.25.4.0662.

Benson, B. B., and D. Krause (1984), The concentration and isotopic fractionation of oxygen dissolved in freshwater and seawater in equilibrium with the atmosphere, *Limnol. Oceanogr.*, *29*(3), 620–632, doi:10.4319/lo.1984.29.3.0620.

Berman-Frank, I., P. Lundgren, Y.-B. Chen, H. Kupper, Z. Kolber, B. Bergman, and P. Falkowski (2001), Segregation of nitrogen fixation and oxygenic photosynthesis in the marine cyanobacterium Trichodesmium, *Science*, *294*(5546), 1534–1537, doi:10.1126/science.1064082.

Corno, G., R. M. Letelier, M. R. Abbott, and D. M. Karl (2006), Assessing primary production variability in the North Pacific subtropical gyre: A comparison of fast repetition rate fluorometry and ^{14}C measurements, *J. Phycol.*, *42*(1), 51–60, doi:10.1111/j.1529-8817.2006.00163.x.

Craig, H., and T. Hayward (1987), Oxygen supersaturation in the ocean: Biological versus physical contributions, *Science*, *235*(4785), 199–202, doi:10.1126/science.235.4785.199.

Doney, S. C. (1996), A synoptic atmospheric surface forcing data set and physical upper ocean model for the U.S. JGOFS Bermuda Atlantic Time-Series Study site, *J. Geophys. Res.*, *101*(C11), 25,615–25,634, doi:10.1029/96JC01424.

Doney, S. C., I. Lima, J. K. Moore, K. Lindsay, M. J. Behrenfeld, T. K. Westberry, N. Mahowald, D. M. Glover, and T. Takahashi (2009), Skill metrics for confronting global upper ocean ecosystem-biogeochemistry models against field and remote sensing data, *J. Mar. Syst.*, *76*(1–2), 95–112, doi:10.1016/j.jmarsys.2008.05.015.

Ducklow, H. W., S. C. Doney, and D. K. Steinberg (2009), Contributions of long-term research and time-series observations to marine ecology and biogeochemistry, *Annu. Rev. Mar. Sci.*, *1*(1), 279–302, doi:10.1146/annurev.marine.010908.163801.

DuRand, M. D., R. J. Olson, and S. W. Chisholm (2001), Phytoplankton population dynamics at the Bermuda Atlantic Time-series station in the Sargasso Sea, *Deep Sea Res., Part II*, *48*(8–9), 1983–2003, doi:10.1016/S0967-0645(00)00166-1.

Eisenstadt, D., E. Barkan, B. Luz, and A. Kaplan (2010), Enrichment of oxygen heavy isotopes during photosynthesis in phytoplankton, *Photosynth. Res.*, *103*(2), 97–103, doi:10.1007/s11120-009-9518-z.

Emerson, S. (1987), Seasonal oxygen cycles and biological new production in surface waters of the subarctic Pacific Ocean, *J. Geophys. Res.*, *92*, 6535–6544, doi:10.1029/JC092iC06p06535.

Falkowski, P. G., and A. D. Woodhead (1992), *Primary Productivity and Biogeochemical Cycles in the Sea*, Springer, Plenum, New York.

Falkowski, P. G., E. A. Laws, R. T. Barber, and J. W. Murray (2003), Phytoplankton and their role in primary, new, and export production, in *Ocean Biogeochemistry*, edited by M. J. R. Fasham, pp. 99–121, Springer, Berlin.

Friedrichs, M. A., et al. (2009), Assessing the uncertainties of model estimates of primary productivity in the tropical Pacific Ocean, *J. Mar. Syst.*, *76*(1–2), 113–133, doi:10.1016/j.jmarsys.2008.05.010.

García, H. E., and L. I. Gordon (1992), Oxygen solubility in seawater: Better fitting equations, *Limnol. Oceanogr.*, *37*, 1307–1312, doi:10.4319/lo.1992.37.6.1307.

Gruber, N., C. D. Keeling, and T. F. Stocker (1998), Carbon-13 constraints on the seasonal inorganic carbon budget at the BATS site in the northwestern Sargasso Sea, *Deep Sea Res., Part I*, *45*(4–5), 673–717, doi:10.1016/S0967-0637(97)00098-8.

Guy, R. D., M. L. Fogel, and J. A. Berry (1993), Photosynthetic fractionation of the stable isotopes of oxygen and carbon, *Plant Physiol.*, *101*(1), 37–47, doi:10.1104/pp.101.1.37.

Halsey, K. H., A. J. Milligan, and M. J. Behrenfeld (2010), Physiological optimization underlies growth rate-independent chlorophyll-specific gross and net primary production, *Photosynth. Res.*, *103*(2), 125–137, doi:10.1007/s11120-009-9526-z.

Hamme, R. C., and S. R. Emerson (2006), Constraining bubble dynamics and mixing with dissolved gases: Implications for productivity measurements by oxygen mass balance, *J. Mar. Res.*, *64*(1), 73–95, doi:10.1357/002224006776412322.

Harrison, W. G., and L. R. Harris (1986), Isotope-dilution and its effects on measurements of nitrogen and phosphorus uptake by oceanic microplankton, *Mar. Ecol. Prog. Ser.*, *27*, 253–261, doi:10.3354/meps027253.

Helman, Y., E. Barkan, D. Eisenstadt, B. Luz, and A. Kaplan (2005), Fractionation of the three stable oxygen isotopes by oxygen-producing and oxygen-consuming reactions in photosynthetic organisms, *Plant Physiol.*, *138*(4), 2292–2298, doi:10.1104/pp.105.063768.

Hendricks, M. B., M. L. Bender, and B. A. Barnett (2004), Net and gross O_2 production in the southern ocean from measurements of biological O_2 saturation and its triple isotope composition, *Deep Sea Res., Part I*, *51*(11), 1541–1561.

Hendricks, M. B., M. L. Bender, B. A. Barnett, P. Strutton, and F. P. Chavez (2005), Triple oxygen isotope composition of dissolved O_2 in the equatorial Pacific: A tracer of mixing, production, and respiration, *J. Geophys. Res.*, *110*, C12021, doi:10.1029/2004JC002735.

Ho, D. T., C. S. Law, M. J. Smith, P. Schlosser, M. Harvey, and P. Hill (2006), Measurements of air-sea gas exchange at high wind speeds in the Southern Ocean: Implications for global parameterizations, *Geophys. Res. Lett.*, *33*, L16611, doi:10.1029/2006GL026817.

Jenkins, W. J., and J. C. Goldman (1985), Seasonal oxygen cycling and primary production in the Sargasso Sea, *J. Mar. Res.*, *43*, 465–491, doi:10.1357/002224085788438702.

Juranek, L. W., and P. D. Quay (2005), In vitro and in situ gross primary and net community production in the North Pacific Subtropical Gyre using labeled and natural abundance isotopes of dissolved O_2, *Global Biogeochem. Cycles*, *19*, GB3009, doi:10.1029/2004GB002384.

Juranek, L. W., and P. D. Quay (2010), Basin-wide photosynthetic production rates in the subtropical and tropical Pacific Ocean determined from dissolved oxygen isotope ratio measurements, *Global Biogeochem. Cycles*, *24*, GB2006, doi:10.1029/2009GB003492.

Kaiser, J. (2011), Technical note: Consistent calculation of aquatic gross production from oxygen triple isotope measurements, *Biogeosciences*, *8*(7), 1793–1811, doi:10.5194/bg-8-1793-2011.

Kaiser, J., and O. Abe (2011), Reply to Nicholson's comment on "Consistent calculation of aquatic gross production from oxygen triple isotope measurements" by Kaiser (2011), *Biogeosciences Discuss.*, *8*(5), 10,517–10,541, doi:10.5194/bgd-8-10517-2011.

Kana, T. M. (1993), Rapid oxygen cycling in *Trichodesmium thiebautii*, *Limnol. Oceanogr.*, *38*(1), 18–24, doi:10.4319/lo.1993.38.1.0018.

Karl, D. M., and R. Lukas (1996), The Hawaii Ocean Time-series (HOT) program: Background, rationale and field implementation, *Deep Sea Res., Part II*, *43*(2–3), 129–156, doi:10.1016/0967-0645(96)00005-7.

Karl, D. M., D. V. Hebel, K. Bjorkman, and R. M. Letelier (1998), The role of dissolved organic matter release in the productivity of the oligotrophic North Pacific Ocean, *Limnol. Oceanogr.*, *43*(6), 1270–1286, doi:10.4319/lo.1998.43.6.1270.

Kiddon, J., M. L. Bender, J. Orchardo, D. A. Caron, J. C. Goldman, and M. Dennett (1993), Isotopic fractionation of oxygen by respiring marine organisms, *Global Biogeochem. Cycles*, *7*(3), 679–694, doi:10.1029/93GB01444.

Kistler, R., et al. (2001), The NCEP-NCAR 50-year reanalysis: Monthly means CD-ROM and documentation, *Bull. Am. Meteorol. Soc.*, *82*(2), 247–267, doi:10.1175/1520-0477(2001)082<0247:TNNYRM>2.3.CO;2.

Knox, M., P. D. Quay, and D. Wilbur (1992), Kinetic isotopic fractionation during air-water gas transfer of O_2, N_2, CH_4, and H_2, *J. Geophys. Res.*, *97*(C12), 20,335–20,343, doi:10.1029/92JC00949.

Kolber, Z. S., O. Prasil, and P. G. Falkowski (1998), Measurements of variable chlorophyll fluorescence using fast repetition rate techniques: Defining methodology and experimental protocols, *Biochim. Biophys. Acta*, *1367*(1–3), 88–106, doi:10.1016/S0005-2728(98)00135-2.

Lämmerzahl, P., T. Röckmann, C. A. M. Brenninkmeijer, D. Krankowsky, and K. Mauersberger (2002), Oxygen isotope composition of stratospheric carbon dioxide, *Geophys. Res. Lett.*, *29*(12), 1582, doi:10.1029/2001GL014343.

Laws, E. A. (1991), Photosynthetic quotients, new production and net community production in the open ocean, *Deep Sea Res., Part A*, *38*(1), 143–167, doi:10.1016/0198-0149(91)90059-O.

Laws, E. A., M. R. Landry, R. T. Barber, L. Campbell, M.-L. Dickson, and J. Marra (2000), Carbon cycling in primary production bottle incubations: Inferences from grazing experiments and photosynthetic studies using ^{14}C and ^{18}O in the Arabian Sea, *Deep Sea Res., Part II*, *47*(7–8), 1339–1352, doi:10.1016/S0967-0645(99)00146-0.

Levine, N. M., M. L. Bender, and S. C. Doney (2009), The $\delta^{18}O$ of dissolved O_2 as a tracer of mixing and respiration in the mesopelagic ocean, *Global Biogeochem. Cycles*, *23*, GB1006, doi:10.1029/2007GB003162.

Luz, B., and E. Barkan (2000), Assessment of oceanic productivity with the triple-isotope composition of dissolved oxygen, *Science*, *288*(5473), 2028–2031, doi:10.1126/science.288.5473.2028.

Luz, B., and E. Barkan (2005), The isotopic ratios $^{17}O/^{16}O$ and $^{18}O/^{16}O$ in molecular oxygen and their significance in biogeochemistry, *Geochim. Cosmochim. Acta*, *69*(5), 1099–1110, doi:10.1016/j.gca.2004.09.001.

Luz, B., and E. Barkan (2009), Net and gross oxygen production from O_2/Ar, $^{17}O/^{16}O$ and $^{18}O/^{16}O$ ratios, *Aquat. Microb. Ecol.*, *56*, 133–145, doi:10.3354/ame01296.

Luz, B., and E. Barkan (2010), Variations of $^{17}O/^{16}O$ and $^{18}O/^{16}$ in meteoric waters, *Geochim. Cosmochim. Acta*, *74*(22), 6276–6286, doi:10.1016/j.gca.2010.08.016.

Luz, B., and E. Barkan (2011), Proper estimation of marine gross O_2 production with $^{17}O/^{16}O$ and $^{18}O/^{16}O$ ratios of dissolved O_2, *Geophys. Res. Lett.*, *38*, L19606, doi:10.1029/2011GL049138.

Luz, B., E. Barkan, M. L. Bender, M. H. Thiemens, and K. A. Boering (1999), Triple-isotope composition of atmospheric oxygen as a tracer of biosphere productivity, *Nature*, *400*(6744), 547–550, doi:10.1038/22987.

Luz, B., E. Barkan, Y. Sagi, and Y. Z. Yacobi (2002), Evaluation of community respiratory mechanisms with oxygen isotopes: A case study in Lake Kinneret, *Limnol. Oceanogr.*, *47*(1), 33–42, doi:10.4319/lo.2002.47.1.0033.

Marra, J. (2002), Approaches to the measurement of plankton production, in *Phytoplankton Productivity: Carbon Assimilation in Marine and Freshwater Ecosystems*, edited by P. J. B. Williams, D. N. Thomas,

and C. S. Reynolds, pp. 78–108, Blackwell Sci., Oxford, U. K., doi:10.1002/9780470995204.ch4.

Marra, J. (2009), Net and gross productivity: Weighing in with ^{14}C, *Aquat. Microb. Ecol.*, *56*, 123–131, doi:10.3354/ame01306.

Marshall, J., et al. (2009), The CLIMODE field campaign: Observing the cycle of convection and restratification over the Gulf Stream, *Bull. Am. Meteorol. Soc.*, *90*(9), 1337–1350, doi:10.1175/2009BAMS2706.1.

Michaels, A. F., and A. H. Knap (1996), Overview of the U.S. JGOFS Bermuda Atlantic Time-series Study and the Hydrostation S program, *Deep Sea Res., Part II*, *43*(2–3), 157–198, doi:10.1016/0967-0645(96)00004-5.

Nicholson, D. P. (2011), Comment on: "Technical note: Consistent calculation of aquatic gross production from oxygen triple isotope measurements" by Kaiser (2011), *Biogeosciences*, *8*(10), 2993–2997, doi:10.5194/bg-8-2993-2011.

Nightingale, P. D., G. Malin, C. S. Law, A. J. Watson, P. S. Liss, M. I. Liddicoat, J. Boutin, and R. C. Upstill-Goddard (2000), In situ evaluation of air-sea gas exchange parameterizations using novel conservative and volatile tracers, *Global Biogeochem. Cycles*, *14*(1), 373–387, doi:10.1029/1999GB900091.

Peterson, B. J. (1980), Aquatic primary productivity and the ^{14}C-CO_2 method: A history of the productivity problem, *Annu. Rev. Ecol. Syst.*, *11*(1), 359–385, doi:10.1146/annurev.es.11.110180.002043.

Price, J. F., R. A. Weller, and R. Pinkel (1986), Diurnal cycling: Observations and models of the upper ocean response to diurnal heating, cooling, and wind mixing, *J. Geophys. Res.*, *91*(C7), 8411–8427, doi:10.1029/JC091iC07p08411.

Prokopenko, M. G., O. M. Pauluis, J. Granger, and L. Y. Yeung (2011), Exact evaluation of gross photosynthetic production from the oxygen triple-isotope composition of O_2: Implications for the net-to-gross primary production ratios, *Geophys. Res. Lett.*, *38*, L14603, doi:10.1029/2011GL047652.

Quay, P. D., D. M. Karl, C. Peacock, and K. M. Bjorkman (2010), Measuring primary production rates in the ocean: Differences between incubation, non-incubation and satellite based methods at Station ALOHA, *Global Biogeochem. Cycles*, *24*, GB3014, doi:10.1029/2009GB003665.

Reuer, M. K., B. A. Barnett, M. L. Bender, P. G. Falkowski, and M. B. Hendricks (2007), New estimates of Southern Ocean biological production rates from O_2/Ar ratios and the triple isotope composition of O_2, *Deep Sea Res., Part I*, *54*(6), 951–974, doi:10.1016/j.dsr.2007.02.007.

Riley, G. A. (1957), Phytoplankton of the north central Sargasso Sea, 1950–52, *Limnol. Oceanogr.*, *2*(3), 252–270.

Robinson, C., G. H. Tilstone, A. P. Rees, T. J. Smyth, J. R. Fishwick, G. A. Tarran, B. Luz, E. Barkan, and E. David (2009), Comparison of in vitro and in situ plankton production determinations, *Aquat. Microb. Ecol.*, *54*(1), 13–34, doi:10.3354/ame01250.

Saba, V. S., et al. (2010), Challenges of modeling depth-integrated marine primary productivity over multiple decades: A case study at BATS and HOT, *Global Biogeochem. Cycles*, *24*, GB3020, doi:10.1029/2009GB003655.

Sarma, V. V. S. S., O. Abe, S. Hashimoto, A. Hinuma, and T. Saino (2005), Seasonal variations in triple oxygen isotopes and gross oxygen production in the Sagami Bay, central Japan, *Limnol. Oceanogr.*, *50*(2), 544–552, doi:10.4319/lo.2005.50.2.0544.

Sarma, V. V. S. S., O. Abe, and T. Saino (2008), Spatial variations in time-integrated plankton metabolic rates in Sagami Bay using triple oxygen isotopes and O_2:Ar ratios, *Limnol. Oceanogr.*, *53*(5), 1776–1783, doi:10.4319/lo.2008.53.5.1776.

Spitzer, W. S., and W. J. Jenkins (1989), Rates of vertical mixing, gas exchange and new production: Estimates from seasonal gas cycles in the upper ocean near Bermuda, *J. Mar. Res.*, *47*(1), 169–196, doi:10.1357/002224089785076370.

Stanley, R. H. R. (2007), A determination of air-sea gas exchange and upper ocean biological production from five noble gases and tritiugenic helium-3, PhD thesis, Jt. Program in Oceangr./Appl. Ocean Sci. and Eng., Mass. Inst. of Technol., Woods Hole Oceanogr. Inst., Woods Hole, Mass.

Stanley, R. H. R., W. J. Jenkins, and S. C. Doney (2006), Quantifying seasonal air-sea gas exchange processes using noble gas time-series: A design experiment, *J. Mar. Res.*, *64*(2), 267–295, doi:10.1357/002224006777606452.

Stanley, R. H. R., W. J. Jenkins, D. E. Lott, and S. C. Doney (2009), Noble gas constraints on air-sea gas exchange and bubble fluxes, *J. Geophys. Res.*, *114*, C11020, doi:10.1029/2009JC005396.

Stanley, R. H. R., J. B. Kirkpatrick, N. Cassar, B. Barnett, and M. L. Bender (2010), Net community production and gross primary production rates in the western equatorial Pacific, *Global Biogeochem. Cycles*, *24*, GB4001, doi:10.1029/2009GB003651.

Steemann Nielsen, E. (1952), The use of radioactive carbon for measuring organic production in the sea, *J. Cons. Int. Explor. Mer*, *18*, 117–140, doi:10.1093/icesjms/18.2.117.

Steinberg, D. K., C. A. Carlson, N. R. Bates, R. J. Johnson, A. F. Michaels, and A. H. Knap (2001), Overview of the US JGOFS Bermuda Atlantic Time-series Study (BATS): A decade-scale look at ocean biology and biogeochemistry, *Deep Sea Res., Part II*, *48*(8–9), 1405–1447, doi:10.1016/S0967-0645(00)00148-X.

Sverdrup, H. U. (1953), On conditions for the vernal blooming of phytoplankton, *ICES J. Mar. Sci.*, *18*, 287–295, doi:10.1093/icesjms/18.3.287.

Sweeney, C., E. Gloor, A. R. Jacobson, R. M. Key, G. McKinley, J. L. Sarmiento, and R. Wanninkhof (2007), Constraining global air-sea gas exchange for CO_2 with recent bomb ^{14}C measurements, *Global Biogeochem. Cycles*, *21*, GB2015, doi:10.1029/2006GB002784.

Thiemens, M. H., T. Jackson, E. C. Zipf, P. W. Erdman, and C. van Egmond (1995), Carbon dioxide and oxygen isotope anomalies in the mesosphere and stratosphere, *Science*, *270*(5238), 969–972, doi:10.1126/science.270.5238.969.

Wanninkhof, R. (1992), Relationship between gas exchange and wind speed over the ocean, *J. Geophys. Res.*, *97*(C5), 7373–7382, doi:10.1029/92JC00188.

Zehr, J. P., and R. M. Kudela (2009), Photosynthesis in the open ocean, *Science*, *326*(5955), 945–946, doi:10.1126/science.1181277.